The Planetary Science Journal, 3:237 (22pp), 2022 October https://doi.org/10.3847/PSJ/ac93f2

Predicting Asteroid Material Properties from a DART-like Kinetic Impact

Kathryn M. Kumamoto[1], J. Michael Owen[1], Megan Bruck Syal[1], Jason Pearl[1], Cody Raskin[1], Wendy K. Caldwell[2], Emma Rainey[3], Angela M. Stickle[3], R. Terik Daly[3], and Olivier Barnouin[3]
[1] Lawrence Livermore National Laboratory, 7000 East Avenue, Livermore, CA 94550, USA; kumamoto3@llnl.gov
[2] Los Alamos National Laboratory, P.O. Box 1663, Los Alamos, NM 87545, USA
[3] Applied Physics Laboratory, Johns Hopkins University, 11100 Johns Hopkins Road, Laurel, MD 20723, USA
Received 2022 August 12; revised 2022 September 16; accepted 2022 September 20; published 2022 October 19

Abstract

NASA's Double Asteroid Redirection Test (DART) mission is the first full-scale test of the kinetic impactor method for asteroid deflection, in which a spacecraft intentionally impacts an asteroid to change its trajectory. DART represents an important first step for planetary defense technology demonstration, providing a realistic assessment of the effectiveness of the kinetic impact approach on a near-Earth asteroid. The momentum imparted to the asteroid is transferred from the impacting spacecraft and enhanced by the momentum of material ejected from the impact site. However, the magnitude of the ejecta contribution is dependent on the material properties of the target. These properties, such as strength and shear modulus, are unknown for the DART target asteroid, Dimorphos, as well as most asteroids since such properties are difficult to characterize remotely. This study examines how hydrocode simulations can be used to estimate material properties from information available post-impact, specifically the asteroid size and shape, the velocity and properties of the impacting spacecraft, and the final velocity change imparted to the asteroid. Across >300 three-dimensional simulations varying seven material parameters describing the asteroid, we found many combinations of properties could reproduce a particular asteroid velocity. Additional observations, such as asteroid mass or crater size, are required to further constrain properties like asteroid strength or outcomes like the momentum enhancement provided by impact ejecta. Our results demonstrate the vital importance of having as much knowledge as possible prior to an impact mission, with key material parameters being the asteroid's mass, porosity, strength, and elastic properties.

Unified Astronomy Thesaurus concepts: Asteroids (72); Impact phenomena (779); Near-Earth objects (1092)

Supporting material: machine-readable table

1. Introduction

Planetary defense preparedness depends upon the ability of space-faring nations to deploy mature mitigation technologies in a timely manner in the event of an Earth-impact emergency. As outlined in the United States' National Near-Earth Object Preparedness Strategy and Action Plan (OSTP 2018), further development of deflection and disruption technologies is required before an imminent threat arises. Kinetic impact is a relatively mature asteroid deflection technology, owing to its simplicity: a spacecraft impacting at many kilometers per second can deliver a significant momentum impulse to an asteroid, through both its own mass and velocity and the additional "boost" of momentum from escaping crater ejecta. As a result of launch vehicle mass limitations, kinetic impact is typically not a viable strategy for shorter warning time scenarios or asteroids that exceed a few hundred meters in diameter (Dearborn & Miller 2015; Dearborn et al. 2020). However, the range of scenarios over which kinetic impact can be effective will partly depend upon the momentum multiplier provided by escaping crater ejecta. For this reason, in addition to demonstrating targeting capabilities and operational readiness, it is desirable to conduct kinetic impact experiments on real asteroids, in which the imparted change in momentum can be well quantified.

Asteroid characteristics that may contribute to uncertainty in an impulsive deflection response include mass, strength, porosity, shape, internal structure, spin state, and equation of state (e.g., Asphaug et al. 1998; Holsapple & Housen 2012; Jutzi & Michel 2014; Bruck Syal et al. 2016; Feldhacker et al. 2017; Raducan et al. 2019, 2020). Currently, a lack of direct data for asteroid material properties, combined with the likely lack of target-specific data on future threats and the observable diversity across the population of near-Earth objects (NEOs), contributes to uncertainty in the momentum multiplication from future kinetic impactor missions. While the constitutive properties of meteorites can be carefully studied in Earth-based laboratories (e.g., Kimberley & Ramesh 2011; Cotto-Figueroa et al. 2016; Moyano-Cambero et al. 2017; Flynn et al. 2018), these samples are biased toward materials that survive atmospheric entry and impact. Additionally, the rubble-pile structures of many NEOs include significant macroporosity, producing bulk geotechnical properties that are likely distinct from the properties of meteoritic hand samples. Both integrated experiments, such as a kinetic impact test with a measurable deflection velocity, and focused science experiments, such as in situ or sample-return characterization, can provide critical ground-truth information for asteroid material properties.

The Asteroid Impact and Deflection Assessment (AIDA) is a collaboration between NASA and ESA to study the effects of impacting an asteroid, increasing Earth's preparedness for potentially hazardous asteroids (Cheng et al. 2015, 2016, 2018). It is composed of NASA's Double Asteroid Redirection Test (DART) mission and ESA's Hera mission, as well as the Light Italian CubeSat for Imaging of Asteroids (LICIACube;

Dotto et al. 2021) carried by DART. In the AIDA collaboration, the DART spacecraft acts as a kinetic impactor, LICIACube follows a few minutes behind to image the ejecta cone soon after impact, and Hera characterizes the asteroid a few years later. DART will impact Dimorphos, the secondary asteroid of the binary system 65803 Didymos. One of the earliest observable consequences of the DART impact will be the change in the orbital period of Dimorphos around the primary asteroid Didymos, which will be measurable from Earth-based telescopes. This change in asteroid velocity is one of the key outcomes of a planetary defense deflection mission, for which the goal would be to nudge the asteroid onto a trajectory that would not impact Earth. DART represents an important planetary defense milestone, as it will carry out Earth's first asteroid deflection test. Interpretation of the DART experiment's results, through modeling and simulation comparison, is essential for estimation of crater ejecta momentum and for the related question of asteroid initial conditions at the impact site.

In support of the DART/AIDA mission, this study presents the results of an inverse test designed to explore the predictive power of the limited information likely available in the weeks following the DART impact. In this test, the Applied Physics Laboratory at Johns Hopkins University (JHUAPL) and Los Alamos National Laboratory (LANL) ran full impact simulations to act as the "truth simulation." The asteroid velocity change resulting from this impact simulation was provided to a team at Lawrence Livermore National Laboratory, along with information regarding the impacting spacecraft, a shape model for the target asteroid, and the impact location on that target, but without any information regarding the target asteroid's material properties. Using this limited data set, we ran impact simulations covering a wide range of material properties to find combinations of parameters that would satisfy the provided velocity change. The inverse test can be viewed as an intensive "dress rehearsal" for impact modelers to prepare for the actual DART experiment, with the truth simulation taking the place of the actual DART impact.

2. Information from the Truth Simulation

For this inverse test, the target asteroid was modeled using a shape model of the asteroid 25143 Itokawa (Fujiwara et al. 2006), shrunken such that the long axis of the asteroid was $\sim$130 m, giving a total volume of $\sim$280,000 m^3 (Figure 1(a)). This shape model was constructed in Daly et al. (2022) from images simulated to match those received from the DART mission, including both the camera on board DART (the Didymos Reconnaissance and Asteroid Camera for Optical navigation, DRACO; Fletcher et al. 2018) and a camera on LICIACube (the LICIACube Explorer Imaging for Asteroid; Dotto et al. 2021). Itokawa was chosen for this inverse test as it is an S-type asteroid like Didymos (and as expected for Dimorphos) and may therefore have similar surface attributes, topography, and characteristics. The aspect ratio of Itokawa, however, is larger than that expected for Dimorphos, resulting in the total volume of the shape model being $\sim$12% of that predicted for Dimorphos.

The truth simulation of the impact was run using two hydrocodes: CTH (McGlaun et al. 1990) at JHUAPL and Free LAGrange (FLAG; Burton 1992, 1994a, 1994b) at LANL. The material properties of the asteroid are presented in Table 1, but parameters such as target strength and porosity were not provided to the inverse modelers since the properties of Dimorphos will also be unknown prior to impact. The spacecraft velocity vector, also used for the simulated DRACO images to construct the shape model (Daly et al. 2022), was slightly oblique to the surface of the target, with a mean angle of 9.5° between the spacecraft velocity and the surface normal at the point of impact. Figures 1(a) and (b) demonstrate the model setup, with the asteroid body in gray and the impactor in red. Using a spacecraft with a mass of 612 kg and relative speed of 7.2 km s^{-1}, the impact caused the body's orbital velocity to decrease by 1.972 ± 0.07 cm s^{-1} in the truth simulation, reducing its orbital period around the primary from ~12 to ~6 hr. For more details regarding the impact site and impact orientation as well as additional information about the truth simulation, please refer to Appendix A.

The work presented here is similar to DART in terms of the data provided from the truth simulation, that is, a shape model for the target asteroid, the location of the impact, and many details regarding the impacting spacecraft. These pieces of information will all be known prior to or developed soon after the DART impact, and the goal of this work is to constrain the target asteroid's properties as much as possible from this limited data set. In this study, we do not include information about the ejecta cone, anticipated from the LICIACube images (Dotto et al. 2021). Thus, we are modeling what can be constrained from the minimum DART mission requirements. The exact numbers used for the inverse test, however, are not the expected values for the actual DART mission. For instance, the spacecraft used here is moving faster than is expected of the DART spacecraft (7.2 km s^{-1} here versus $\sim$6.1 km s^{-1} for the DART impact; Stickle et al. 2022). The extra hard hit from the spacecraft combined with the small volume of the shape model leads to a period change given for the inverse test that is almost 50% of the orbital period of Dimorphos, a value large enough to catastrophically affect the stability of the binary system. In the actual DART impact, the velocity change for Dimorphos is expected to be a few millimeters per second or less, rather than centimeters per second. However, while the numbers and shape model used in this study differ from those expected for the DART mission, all provided data are representative of the types of information made available shortly after the DART impact in 2022 September, and future interventions on potentially hazardous asteroids may require extreme deflections similar to this study.

3. Spheral Models

3.1. Spheral

We performed our impact calculations using Spheral, an open-source Adaptive Smoothed Particle Hydrodynamics code maintained by Lawrence Livermore National Laboratory (https://github.com/LLNL/spheral; Owen et al. 1998; Owen 2010). The simulation setup as well as two example simulations are shown in Figure 1. Spherals elastic–perfectly plastic formulation and approach to modeling material fracture is adapted from Benz & Asphaug (1994). We model the fracture using a tensor-based generalization of the statistical damage model of Grady & Kipp (1980), which accounts for the decrease in tensile strength with increasing volume. To model yield strength, we use a modified form of the of the pressure-dependent approach of Collins et al. (2004), which accounts for the increase in yield strength with confining pressure. To model porous compaction, we use the strain–porosity model of Wünnemann et al. (2006) with the thermal correction of Collins et al. (2011).

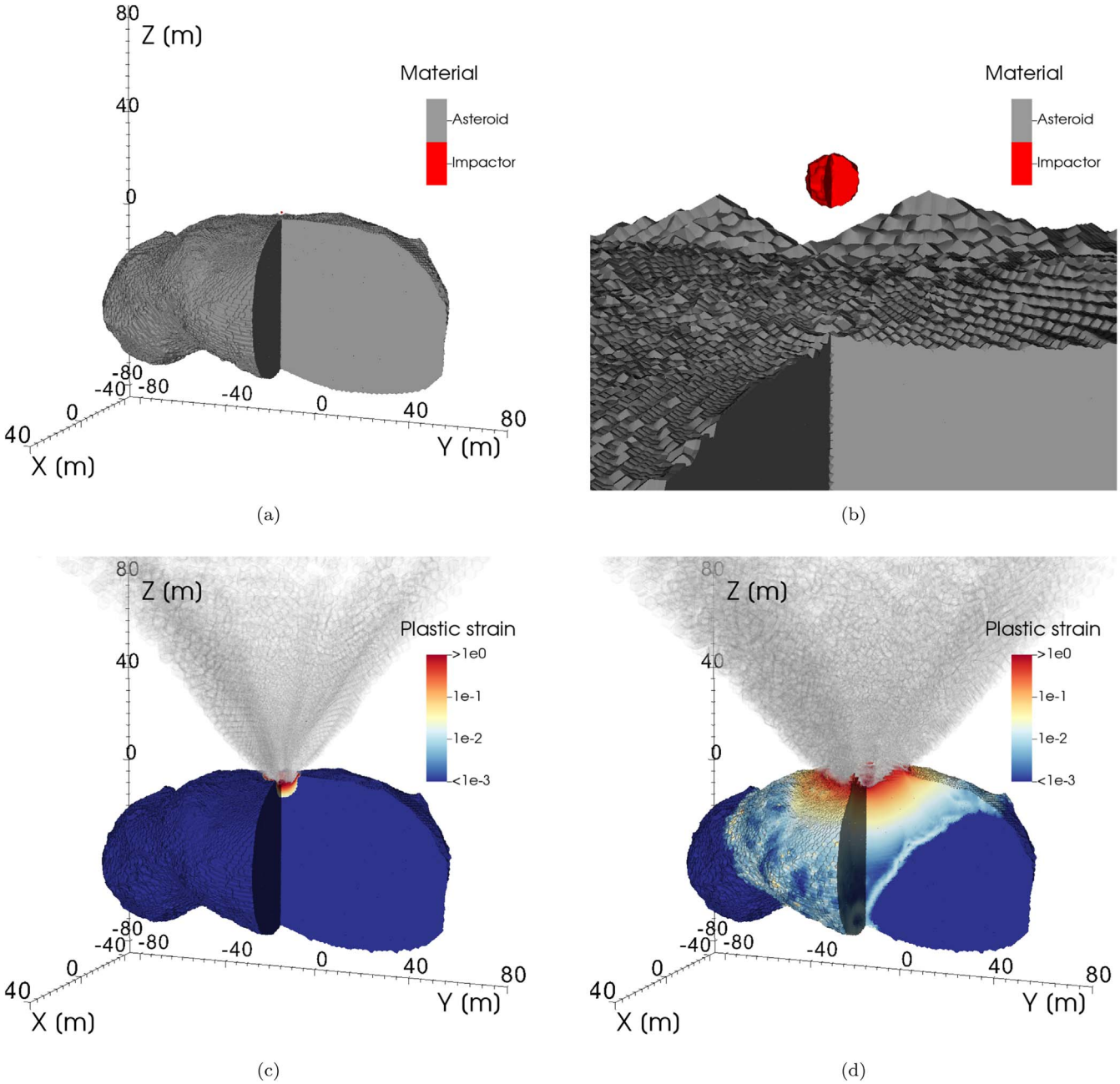

Figure 1. Example visualizations of the Spheral simulations. One quadrant is clipped out of the simulation to show the interior structure of the asteroid. (a) The setup for our simulations. The asteroid body is in gray, and the impactor is in red. (b) Same as in (a) but zoomed in on the impactor. (c) The results from simulation 11.09. The asteroid is colored by plastic strain, and low-density ejecta is translucent gray. This simulation had a relatively strong and porous asteroid body. (d) The results from simulation 22.05. Colors are the same as in (c). This simulation had a relatively weak asteroid body with low porosity.

We simulate the impact in three spatial dimensions. The resolution of the simulations is 10 cm at the impact point and decreases outward in spherical shells, with spacing between particles increasing by a ratio of 1.01 in successive shells. This resolution equates to 3 nodes per impactor radius. Particle mass, volume, and smoothing length all vary consistent with this initial graded particle distribution and the appropriate initial density. For additional information regarding the Spheral models and material parameters used in these models, please refer to Appendix B.

We made a few simplifying assumptions to define the initial conditions of our simulations. First, the impactor was modeled as a solid aluminum sphere (Figure 1(b)). The asteroid was modeled as a single isomorphic, homogeneous, microporous body of SiO_2 using an SiO_2 equation of state (EOS) from the Livermore Equation of State (LEOS) database (Fritsch 2016). The choice of SiO_2 as our material is not especially unusual as quartz is a well-explored material in mineral physics, though we also briefly examine the use of basalt, granite, and pumice as asteroid materials, in addition to using both the ANEOS (Thompson 1990) and Tillotson EOS (Tillotson 1962). Aside from the simulations testing different materials, the density of fully solid material (i.e., porosity = 0) was held constant between simulations at 2.65 g cm^{-3}, which is the density of SiO_2 at ambient Earth conditions.

We varied seven variables describing the asteroid's material properties: the solid yield strength of intact and damaged

Table 1
Ranges of Input and Output Values for Truth Simulations and Inverse Simulations

	Truth Simulation		All Inverse Simulations		Simulation Subset $\Delta V = -1.972 \pm 0.07$ cm s^{-1}		Simulation Subset $\Delta V = -1.972 \pm 0.07$ cm s^{-1} $M_A = 599, 758 \pm 59, 976$ kg ($\phi = 0.18 \pm 0.08$)	
	CTH	FLAG						
n	1	1	338		37		12	
			Minimum	**Maximum**	**Minimum**	**Maximum**	**Minimum**	**Maximum**
Y_{s0} (MPa)	1.00e+1	1.00e+1	1.00e−3	1.50e+2	5.01e−3	1.46e+2	5.01e−3	1.07e+2
Y_{d0} (MPa)	⋯	⋯	1.00e−5	1.00e+0	1.02e−3	9.52e−1	3.80e−3	6.92e−2
G_{s0} (MPa)	⋯[a]	2.90e+3	1.00e+1	1.00e+5	1.07e+1	1.00e+5	1.07e+1	1.02e+4
G_{d0} (MPa)	⋯	⋯	1.00e−1	1.00e+3	1.45e−1	9.91e+2	1.45e−1	9.55e+2
ϕ	0.24	0.24	0.05	0.70	0.11	0.6	0.11	0.25
$-P_{min}$ (MPa)	⋯	⋯	1.00e−5	1.00e+2	1.45e−5	8.13e+1	3.09e−5	8.13e+1
$-P_{d,min}$ (MPa)	⋯	⋯	0	1.00e−4	0	9.55e−2	1.15e−7	9.55e−2
ΔV (cm s^{-1})	−2.02	−1.92	−0.89	−4.60[b]	−1.90	−2.04	−1.91	−2.04
β	3.3	3.5	1.4	6.9[b]	1.53	3.59	2.88	3.59
W_c (m)	9.2[c]	⋯	⋯	⋯	11.3	47.0	19.2	47.0
D_c (m)	6.9[c]	⋯	⋯	⋯	3.6	15.9	4.9	14.4

Notes. The truth simulation parameters were unknown to the inverse team when inverse simulations were being run, but they are included here for ease of comparison. The total inverse simulation population is broken down into subsets meeting specific constraints. For each subset, the criteria for selection are listed in the header and the corresponding range of material properties are shown. Crater width and crater depth were only calculated for simulations with the correct ΔV, so ranges are not reported for the whole simulation set.
[a] While an intact shear modulus was not set in the CTH simulation, the Poisson's ratio was set to 0.25.
[b] Does not include values for simulation with fluid-like behavior.
[c] Transient crater measured at 0.1 s.

material (Y_{s0} and Y_{d0}), the solid shear modulus of intact and damaged material (G_{s0} and G_{d0}), the minimum pressure (i.e., maximum tensile pressure) allowed in intact (P_{min}) and damaged ($P_{d,min}$) material, and the initial porosity of the starting material (ϕ). Properties for damaged materials were constrained to be smaller in magnitude than their intact equivalents (e.g., $Y_{d0} < Y_{s0}$), but otherwise, parameters were allowed to vary independently. Specific ranges searched for each variable are in Table C1.

3.2. Simulation Metrics

There were three key results from each simulation: ΔV for the asteroid in the orbital direction, the momentum enhancement factor describing the contribution of the ejecta to asteroid momentum (β), and the crater morphology. Ejecta was defined as material at least 1 m away from the asteroid surface and moving faster than 5 cm s^{-1} away from the centroid of the asteroid (Figure B1; see Appendix B.2 for more detail). ΔV was calculated from the momentum of the impacting spacecraft (ρ_s), the momentum of the ejecta (ρ_e), and the mass of the asteroid (M_A):

$$\Delta V = \frac{(\boldsymbol{\rho}_s + \boldsymbol{\rho}_e) \cdot \hat{\boldsymbol{o}}}{M_A}, \tag{1}$$

in which the subscripts "A," "s," and "e" refer to the asteroid, spacecraft, and ejecta, respectively. The unit vector in the orbital direction is denoted as $\hat{\boldsymbol{o}}$.

The momentum enhancement factor β is a multiplicative factor applied to the spacecraft momentum to express the contribution of impact ejecta to asteroid momentum. In its simplest form, β is the ratio of the momentum of the asteroid after impact to the initial momentum of the impacting spacecraft. In this study, β was calculated using the definition for momentum enhancement in the orbital direction described in Rivkin et al. (2021):

$$\beta = \frac{(M_A/M_s)\Delta V_{A,o} - \boldsymbol{V}_{s,\perp\hat{n}} + V_{s,n}\boldsymbol{\epsilon} \cdot \hat{\boldsymbol{o}}}{V_{s,n}(\hat{\boldsymbol{n}} + \boldsymbol{\epsilon}) \cdot \hat{\boldsymbol{o}}}. \tag{2}$$

In this equation, M_A is the mass of the asteroid, M_s is the mass of the impacting spacecraft, $\hat{\boldsymbol{n}}$ is the surface normal unit vector, and $\boldsymbol{\epsilon}$ is the offset vector between $\hat{\boldsymbol{n}}$ and the velocity vector of the ejecta. $\Delta V_{A,o}$ is the change in the asteroid's velocity in the orbital direction (simply referred to as ΔV for the remainder of the paper). $\boldsymbol{V}_s$ refers to the velocity of the impacting spacecraft and is broken down into the magnitude of velocity parallel to the surface normal for $V_{s,n}$ and the velocity vector perpendicular to the surface normal (along the surface) for $\boldsymbol{V}_{s,\perp\hat{n}}$.

The width (W_c) and depth (D_c) of the impact crater was measured for successful simulations (i.e., those that produced a ΔV in the range dictated by the truth simulation). Crater formation occurs over times on the order of minutes to hours rather than the fractions of a second to seconds typically run in hydrocodes. To predict the final crater as accurately as possible from the final time steps of our successful simulations (from 0.6 up to 3.1 s, depending on the simulation), we applied a density constraint such that material with a density less than 95% of the original porous density of the asteroid was assumed to eventually leave the crater. We use this metric, as material in this state is typically under tension and in the process of being evacuated from the growing transient crater. For relatively small craters with diameters less than 20 m, crater sizes were calculated by fitting the cratered region of the asteroid with a plane describing the asteroid surface and a hyperboloid describing the crater (Figure B2; Klein 2013). For larger craters, crater depth and diameter were measured by hand.

3.3. Efficiently Covering Search Space Using Machine Learning and Extrapolation

The large dimensional space associated with the seven input variables placed constraints on our available computational time, requiring an efficient methodology to adequately constrain the parameter space. Two main techniques were used to mitigate the computational cost (additional details for both can be found in Appendix C). First, we used a machine-learning decision-tree algorithm to select parameter combinations. We initialized the tree with a preliminary run of 40 simulations with randomized input parameters. For each subsequent run, between three and 16 simulations were chosen from 10,000 possible solutions, using the Mitchell's Best Sampling algorithm (Mitchell 1991) to select the parameter combinations covering the largest parameter space in our seven dimensions.

Second, while the ideal case would be to run all of our simulations until stable values of β and ΔV were reached, as well as stable crater formation, the size of our data set makes this approach prohibitively computationally expensive. Thus, as the truth model provided a relatively narrow target range for ΔV of $\pm 0.07\ \mathrm{cm\ s^{-1}}$, simulations that clearly overshot or undershot the velocity range were terminated prior to ΔV and β stabilizing. The relationship between ΔV and time was extrapolated using an exponential decay model, taking the infinite time limit as the stable ΔV (see Figure D1 for all simulation fits; see Appendix D for more detail). For simulations with high porosity, a local maximum in ΔV was often observed at small times ($t \sim 0.1$–0.3 s). For the purposes of extrapolation, this local maximum was fit phenomenologically by adding a Gaussian peak to the exponential decay model. β was extrapolated in the same way, with or without an additional Gaussian peak depending on the porosity in the simulation. Simulations with values of ΔV close to the target ΔV were run until relatively stabilized (i.e., with a small $\delta V/\delta t$).

4. Results

4.1. Trends across All Simulations

We ran 338 simulations covering a wide range of input parameters. The results of these simulations are summarized in Figure 2, the ranges of inputs and outputs covered are listed in Table 1, and all inputs and deflection results can be found in Table F1. For clarity, we plot ΔV as its magnitude, but all values of ΔV are negative in our simulations (i.e., the asteroid orbital period decreases after impact).

One of the largest individual effects on ΔV comes from porosity, with larger values of ΔV associated with more porous targets (Figure 2). This observation is predominantly a result of the effect of porosity on the total initial mass of the asteroid, as asteroid volume and solid density (i.e., density at 0% porosity) were constant between simulations. The momentum of the impacting spacecraft is constant between simulations. Thus, neglecting any effect of impact ejecta, conservation of momentum results in the velocity change of the asteroid being larger when the asteroid has less mass. This effect can be observed in the positive relationship between porosity and ΔV, particularly for high values of porosity.

Strength and shear modulus for both intact and damaged material have negative correlations with ΔV (Figure 2), meaning that simulations with yield strengths and shear moduli that more closely approximate fully intact rock are more likely to result in small velocity changes. At the other extreme, simulations that resemble weak dry sediment or sand are more likely to have large velocity changes. Previous work examining the effects of yield strength or cohesion on ΔV and β also observed these correlations (e.g., Bruck Syal et al. 2016; Raducan et al. 2019).

P_{min} and $P_{\mathrm{d,min}}$ do not have strong effects on ΔV across the simulations. There is essentially no correlation between the magnitude of P_{min} and ΔV and only a shallow positive correlation between the magnitude of $P_{\mathrm{d,min}}$ and ΔV across 6 orders of magnitude (Figure 2). To quantify these relationships (or lack thereof), we ran a Monte Carlo regression model, in which we fit a regression to a subset of our data set 10,000 times and took the average and standard deviation of those 10,000 results. For the trends of both P_{min} and $P_{\mathrm{d,min}}$ versus ΔV, the standard deviation of the regression results for the slope is larger than the average slope, suggesting that any trend observed is statistically insignificant. The general lack of a trend between P_{min} and $P_{\mathrm{d,min}}$ and the resulting deflection suggests that tensile stresses in our simulations are not controlling the overall deflection response of the asteroid.

As the mass of the asteroid is not constant between simulations, there is not a linear relationship between ΔV and β (Figure 3), but the two are positively correlated through the general equation for β (Equation 2). In fact, for most variables, the trends observed with ΔV and β are the same, i.e., both positive, both negative, or both essentially negligible (Figure 2). The one exception is porosity. The correlation between ϕ and ΔV is positive, as high-porosity targets have lower mass. However, there is a negative relationship between porosity and β. In more porous targets, a larger portion of the kinetic energy of the impactor goes toward compaction of the target material rather than the ejection of material. These results are consistent with previous work examining the effects of porosity on asteroid deflection (e.g., Bruck Syal et al. 2016; Stickle et al. 2017; Raducan et al. 2019).

4.2. Defining Realistic Targets

Our data set covers a large range of properties, and it is worth emphasizing that we did little to control the realism of material parameter combinations. While this methodology allows us to easily and effectively explore the parameter space, some simulations are not predictive for real asteroids that might be encountered. It is thus instructive to examine trends in subsets of data that are more representative of real material.

4.2.1. Strong and Weak Targets

Figure 2 uses the intact asteroid strength and shear modulus to define realistic combinations representing strong and weak target material. Simulations shown in red in Figure 2 are a subset with large intact strength and shear moduli more consistent with rock ($Y_{s0} > 10$ MPa, $G_{s0} > 10$ GPa). Simulations in blue represent weaker material more consistent with fractured rock or sediment ($Y_{s0} < 10$ MPa, $G_{s0} < 10$ GPa). Finally, simulations in white are simulations in which one intact parameter is large while the other intact parameter is small (e.g., large Y_{s0} and small G_{s0}), combinations which are unlikely to occur. We do not include porosity in this comparison.

In both the strong and weak subsets, the trends between porosity and ΔV are much clearer for intermediate and very porous materials ($\phi > 20\%$) than the trend for the whole data set. For the same porosity, weak target material generally results in a larger ΔV compared to stronger target material,

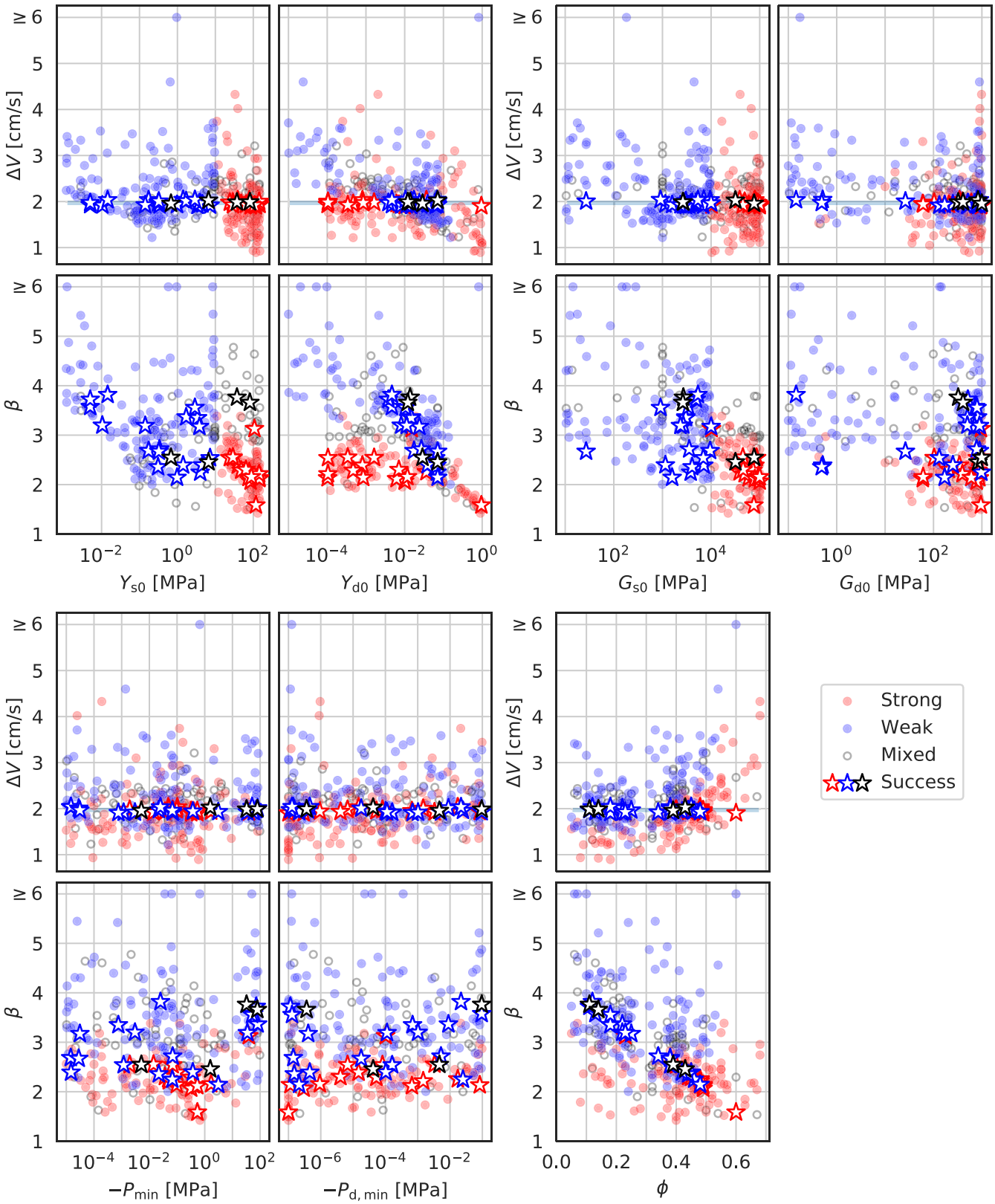

Figure 2. Results of all simulations. Final ΔV and β are extrapolated to $t = \infty$. Simulations with $Y_{s0} > 10$ MPa and $G_{s0} > 10$ GPa are colored in red and are more consistent with strong, intact rock. Simulations with $Y_{s0} < 10$ MPa and $G_{s0} < 10$ GPa are colored in blue and are more consistent with weak, fractured rock or sediment. Simulations in open gray circles have either a large Y_{s0} and a low G_{s0}, or a low Y_{s0} and a large G_{s0}. Simulations with final ΔV values in the target range are denoted with stars. Simulations with $P_{d,min} = 0$ are plotted at 10^{-7} MPa.

aligning with the overall trends observed for the full data set (Figure 2). Similarly, weak target material generally results in a larger β for the same porosity.

For the initially strong, more rock-like simulations (in red), there is not a strong trend between ΔV and the variables for damaged material (Y_{d0} and G_{d0}) (Figure 2). The lack of a trend

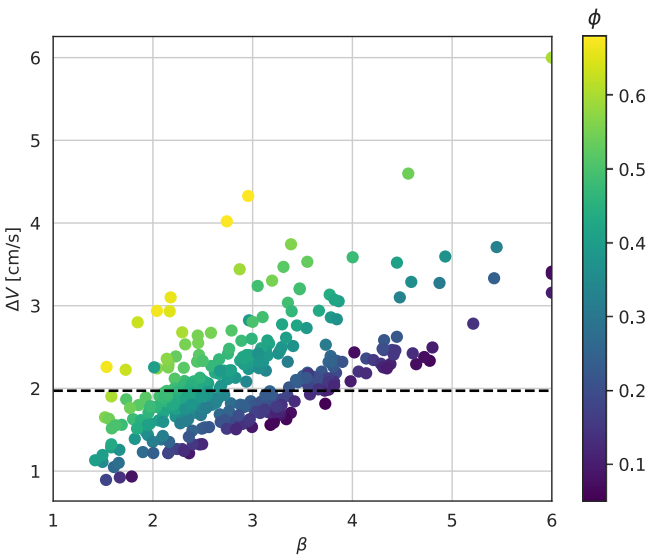

Figure 3. Final ΔV vs. β for all simulations. Each simulation is colored by initial porosity, ϕ. The target ΔV of $-1.972\,\mathrm{cm\,s^{-1}}$ is indicated with a dashed line.

is particularly evident for Y_{d0}: the simulations in red at low Y_{d0} cover ranges of values for ΔV and β similar to simulations at high Y_{d0}, particularly for $Y_{d0} < 10^{-1}$ MPa. In contrast, when Y_{s0} and G_{s0} are both small, ΔV and the damaged variables (Y_{d0} and G_{d0}) have strong negative correlations. These relationships suggest that the ejecta response for strong asteroid targets is controlled by the initial material parameters (Y_{s0} and G_{s0}), and the initial yielding of asteroid material is the limiting step in ejecta formation. For initially weak asteroid targets, on the other hand, the ejecta response is controlled by the parameters for damaged material (Y_{d0} and G_{d0}), and the deformation of material that is already damaged controls the ejecta formation.

4.2.2. Realistic Elastic Parameters

We searched a large range of shear moduli, but we note that we did not directly link the bulk modulus to the prescribed shear modulus. Instead, the bulk modulus for each simulation was calculated from the SiO_2 EOS. As a result, the Poisson's ratio (ν) of our simulations varied substantially. Simulations with low shear moduli had very large Poisson's ratios, close to the maximum value of 0.5. By comparison, porous rhyolitic lavas (up to $\phi = 0.5$) also demonstrate Poisson's ratios of up to $\sim$0.45 (e.g., Mordensky et al. 2018; Ji et al. 2019). Vacuum-saturated beach sands demonstrate a large range of Poisson's ratios but have a maximum of 0.42 for typical grain sizes of hundreds of micrometers to around a millimeter (Kimura 2006). Poisson's ratios larger than $\sim$0.45 in geologic material, however, are uncommon without introducing pore fluids (e.g., Kimura 2006), which are unrealistic for asteroid environments.

At the other extreme, simulations with extremely large shear moduli require auxetic behavior with negative Poisson's ratios. Auxetic materials generally have very low densities resulting from their complex open structures (e.g., Alderson & Alderson 2007), and they are exceedingly rare in geologic materials. Alpha-cristobalite, a high-temperature polymorph of SiO_2, is the only known natural mineral with a negative Poisson's ratio (Ji et al. 2018), though some artificial pumice analogs have been reported to have negative Poisson's ratios as well (Wollner et al. 2018).

Examining only the simulations with solid Poisson's ratios similar to typical geologic material (0–0.45), the trends we observe across simulations do not change (Figure F1). The ranges of material parameters for successful simulations are similarly unaffected, aside from the solid shear modulus, as it is directly constrained by the Poisson's ratio. Given the generally unchanged results, we will consider all simulations, including those with extreme Poisson's ratios, in the remainder of the manuscript.

5. Predicting Asteroid Properties

5.1. Matching ΔV

Thus far, we have discussed the trends observed across all of our simulations. However, the goal of the simulation efforts presented here is to find material parameter combinations that produce a particular ΔV, in this case $-1.972\,\mathrm{cm\,s^{-1}}$. These solutions are shown as stars in Figure 2 and as white lines in Figure 4. The minimum and maximum values for each variable for successful simulations (i.e., those simulations with $\Delta V = -1.972 \pm 0.07\,\mathrm{cm\,s^{-1}}$) are reported in Table 1. Example visualizations of simulations that produced the correct ΔV with very different material parameters are shown in Figures 1(c)–(d).

Looking at material parameters in isolation, the successful simulations cover a large range of properties. In line with the small effect of these variables on ΔV, both P_{min} and $P_{d,min}$ for successful simulations cover nearly the entire range of search space. Porosities for successful simulations are in the range of 11%–60%. This range covers everything from roughly intact rock up to the porosities observed in rubble-pile asteroids like Itokawa or 101955 Bennu (Walsh 2018). The large range in asteroid mass associated with these porosities leads to a range of values for β of 1.5–3.6.

Maximum values for Y_{s0} and G_{s0} for these simulations are representative of strong rock ($Y_{s0} = 146$ MPa, $G_{s0} = 100$ GPa). Minimum values ($Y_{s0} = 174$ kPa, $G_{s0} = 27$ MPa) are similar to the cohesion and shear modulus for clay (Onur et al. 2014). The strength and shear modulus for damaged material in successful simulations are also similar to the properties of sediment. Y_{d0} varies from 100 Pa to 71 kPa, covering a range similar to that expected for lunar regolith (Holsapple & Housen 2012) or the surface of the rubble-pile asteroid 162173 Ryugu (Arakawa et al. 2020). With the exception of two simulations with G_{d0} of $\sim$500 kPa and one simulation with G_{d0} of $\sim$150 kPa, the shear moduli for damaged material range from $\sim$30 MPa to $\sim$1 GPa, demonstrating elasticity similar to sand on the low end of that range (Onur et al. 2014). Shear moduli of $\leqslant$500 kPa, however, are quite small for geologic material, and nearly all of the simulations with similar shear moduli for damaged material result in velocity magnitudes larger than the target ΔV. One simulation with $G_{d0} \sim 200$ kPa, in addition to low strength and G_{s0}, even exhibited fluid-like behavior (Figure E1). While examining low values for G_{d0} was helpful for establishing the algorithmic search space, this behavior is extremely unlikely for actual asteroid material.

5.2. Reproducing the Truth Simulation Material Parameters

The results from the truth simulation were defined using the average of results from two different codes: CTH (McGlaun et al. 1990) and FLAG (Burton 1992, 1994a, 1994b). These simulations were run to a final time of 0.1 s in CTH and 0.2 s in FLAG. Both simulations used a basalt EOS, SESAME (Lyon & Johnson 1992)

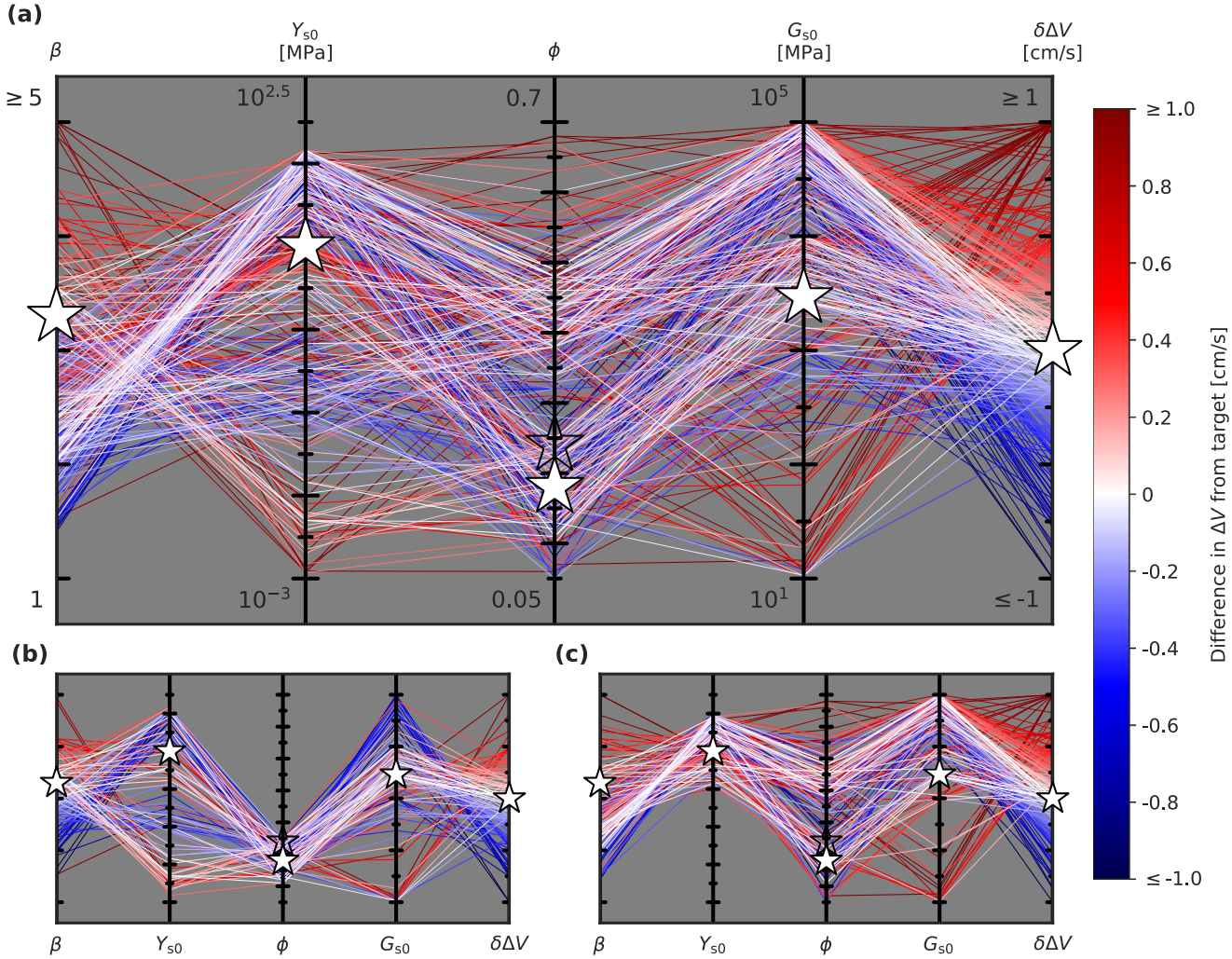

Figure 4. Parallel coordinate plots of input parameters with equivalent parameters in the truth simulations, as well as final ΔV and β. Simulation lines are colored by the difference between the simulation ΔV and the target ΔV, with blue being slower than the truth simulation and red being faster than the truth simulation. White stars indicate the values of the truth simulation. For ϕ, the open star indicates the original truth simulation value of 0.24 while the solid white star indicates the porosity required for an equivalently massive asteroid in our simulations. Plots are shown for (a) all simulations, (b) simulations with initial asteroid mass within 10% of the truth simulation, and (c) simulations with Y_{s0} within 1 order of magnitude of the truth simulation. Ticks and axis limits in (b) and (c) are the same as in (a).

for CTH or Mie-Grüneisen (Meyers 1994) for FLAG, to describe the asteroid material, with a yield strength of 10 MPa, a density of 2.855 g cm^{-3} for fully solid material, and a porosity of 24% (and thus a bulk density of 2.170 g cm^{-3}). The FLAG simulation explicitly set a shear modulus for intact material of 2.9 GPa while the CTH simulation set a Poisson's ratio of 0.25. The average β resulting from the CTH and FLAG truth simulations was 3.4. These parameters are listed in Table 1, and additional detail about the truth simulation codes can be found in Appendix A. Figure 4 compares the inverse simulations to the truth simulation in a parallel coordinate plot, with the truth simulation parameters plotted as stars. (For a parallel coordinate plot of all of the input parameters used in the Spheral simulations, see Figure F2 in Appendix F.)

With the wide range of parameters covered by our successful simulations, the truth simulation parameters fall inside the ranges described in the previous section (Figure 4(a)). Indeed, several of our parameter combinations are quite close to the truth simulation. However, solutions with similar parameters are uncommon overall. For instance, values of Y_{s0} within 1 order of magnitude of the truth simulation value of 10 MPa are associated with both low and high porosities, with higher porosities generally correlated with larger shear moduli (Figure 4(c)). Looking at the inverse correlation, successful simulations with low porosities, and thus asteroid masses similar to the truth simulation, are associated with both high strengths in the range of megapascals and low strengths of a few kilopascals (Figure 4(b)).

Beyond the multisolution degeneracy of the problem of asteroid deflection, there are several potential explanations for why the parameter combination from the truth simulation is uncommon in our inverse simulations. First, there are inherent differences in the way different hydrocodes process impact problems. Each code in this study utilizes a different discretization method: CTH is an Eulerian finite-difference code, FLAG is an arbitrary Lagrange-Eulerian finite-volume code, and Spheral is a smoothed particle hydrodynamics code. There are also other implementation aspects that differ between the three codes. For example, once material is fully damaged in both the CTH and FLAG simulations, it can no longer support any stress. Conversely, the Spheral simulations explicitly set both a strength (Y_{d0}) and a shear modulus (G_{d0}) for fully damaged material (see Owen et al. 2022 for additional details regarding the damage model in Spheral). Thus, Spheral

simulations with the same parameters describing intact material as the truth simulation (i.e., Y_{s0}, G_{s0}, and ϕ) could have smaller values for ΔV and β due to the contribution of nonzero values of Y_{d0} and G_{d0}. Even when great effort is made to make sure hydrocodes are working on as identical a problem as possible (e.g., by constraining material parameters, equations of state, and strength models), there are still differences in final simulation results with variations in β of 15%–20% between the different codes (Stickle et al. 2020).

For the inverse test, we used the differences between codes to model the imperfections of using our hydrocodes to simulate reality. As the truth simulation was only a model itself, however, we can further examine the CTH, FLAG, and Spheral simulations to pull apart some of the more minute differences. For instance, in benchmarking tests using a basalt EOS to describe the target, CTH predicts larger values of β (and thus larger values of ΔV) than Spheral for targets with the same properties (Stickle et al. 2020). Applying this difference to the inverse problem described in this study suggests that replicating the truth simulation parameters in Spheral would result in a smaller β and ΔV than the CTH results. Thus, in order to reproduce the correct ΔV with an asteroid mass close to the truth simulation, more of our successful simulations have lower values of Y_{s0} (Figure 4(b)). Conversely, many successful simulations with Y_{s0} close to 10 MPa have higher porosities than the truth simulation (Figure 4(c)).

We also consider the simulation time at which ΔV is measured or estimated. The truth simulation reported ΔV at $t = 0.1$ s and 0.2 s after impact, while we extrapolate ΔV to $t \sim \infty$. If we compare the ΔV at 0.1 s ($\Delta V_{0.1}$) with the extrapolated infinite-time ΔV (ΔV_{∞}) for our simulations, the extrapolated ΔV is nearly always larger than $\Delta V_{0.1}$ (Figure 5). This observation also holds for ΔV measured at 0.2 s ($\Delta V_{0.2}$). The exceptions are generally simulations for strong targets, where a local maximum is observed in ΔV at early times. Since ΔV_{∞} was larger than $\Delta V_{0.1}$ for most simulations, simulations with $\Delta V_{0.1} = -1.972 \pm 0.07$ cm s^{-1} were generally shifted to weaker targets (i.e., targets with larger ΔV_{∞}) compared to simulations in which ΔV_{∞} was in the target velocity range.

An additional discrepancy between the truth simulation and our Spheral simulations was the choice of EOS. Our choice of LEOS SiO_2 for the asteroid material does not match the SESAME or Mie-Grüneisen basalt EOS used in the truth simulation. To briefly explore the effect of EOS and material choice, we chose four of our successful simulations covering a range of material property combinations. We reran these simulations using different choices for asteroid material and EOS while keeping the seven input material properties (i.e., Y_{s0}, Y_{d0}, etc.) the same. The EOS/material combinations we tested were Tillotson basalt, Tillotson granite, Tillotson pumice, and ANEOS SiO_2 (Tillotson 1962; Thompson 1990).

Variability in β resulting from the choice of EOS and material for the asteroid is 10%–16% (Figure 6, Table F2), consistent with previous observations (Bruck Syal et al. 2016; Stickle et al. 2017). Variability in ΔV is much larger (up to 26%), predominantly because of the varying nonporous densities of the different EOS and material options. However, when only considering the SiO_2, basalt, and granite EOS options, which all have similar nonporous densities, variability in ΔV is 8%–14%, comparable to the variability in β. The LEOS and ANEOS SiO_2 results are similar to each other both in terms of β as well as ΔV, and the Tillotson EOS have similar values of β (Figure 6). Interestingly, the different asteroid EOS and material combinations are not consistent in their distribution. For instance, using Tillotson granite to describe the asteroid resulted in the smallest ΔV and β for the two strongest cases tested here (1–4 and 9–0), but ANEOS SiO_2 had the smallest ΔV and β for the two weakest cases (22–5 and 11–9).

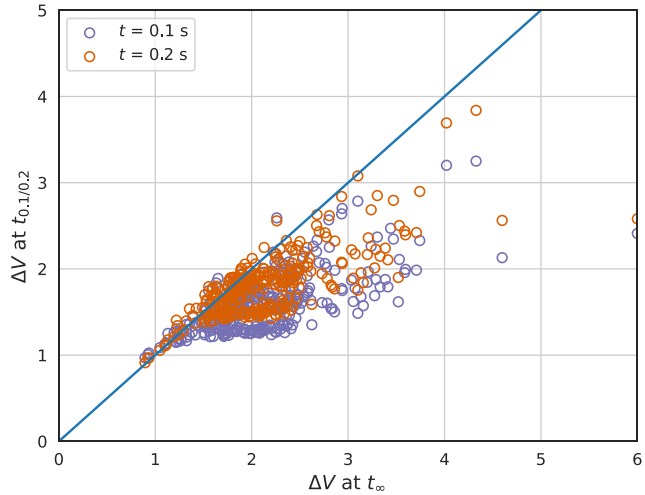

Figure 5. ΔV at $t = 0.1$ s (purple) or $t = 0.2$ s (orange) vs. ΔV at $t \sim \infty$. The blue line is 1:1.

5.3. Constraints from Hera after Impact

Additional constraints for the DART impact will be provided by Hera when it reaches the Didymos system in 2026. Hera will measure the mass of Dimorphos, with an expected accuracy of at least 10% (Michel et al. 2018). Figure 4(b) demonstrates that we have three main populations of values for Y_{s0} when constraining the mass of the target asteroid: tens of megapascals, a few megapascals, or a few kilopascals. Remarkably, however, the shear modulus for all successful mass-constrained simulations is within approximately 0.5 an order of magnitude of the truth simulation. The ranges for different input variables of successful solutions when constrained by asteroid mass are in Table 1.

In addition to mass, Hera will also measure the size of the impact crater left by DART. The morphology of the residual crater after an impact is expected to vary substantially with material properties (e.g., Holsapple & Housen 2012), and we observe a wide variety of crater sizes among successful simulations (Figure 7, Table F3). In general, both crater width and crater depth are inversely correlated with Y_{s0} (Figure 7(a)). The crater width in the x-direction and the crater width in the y-direction are typically close, though not the same. Small craters generally have slightly wider widths in the y-direction, likely due to the mild obliquity of the impact interacting with the topography of the impact location. For larger craters, there are examples with the width in the x-direction being larger as well as examples with width in the y-direction being larger. This variation is at least in part a result of the complicated crater shapes predicted for these simulations. In addition, for a given Y_{s0} (or narrow range of values for Y_{s0}), crater width decreases with increasing porosity. The ratio of crater width to crater depth is also correlated with porosity, with impacts into more porous asteroids generating craters with lower aspect ratios (Figure 7(b)).

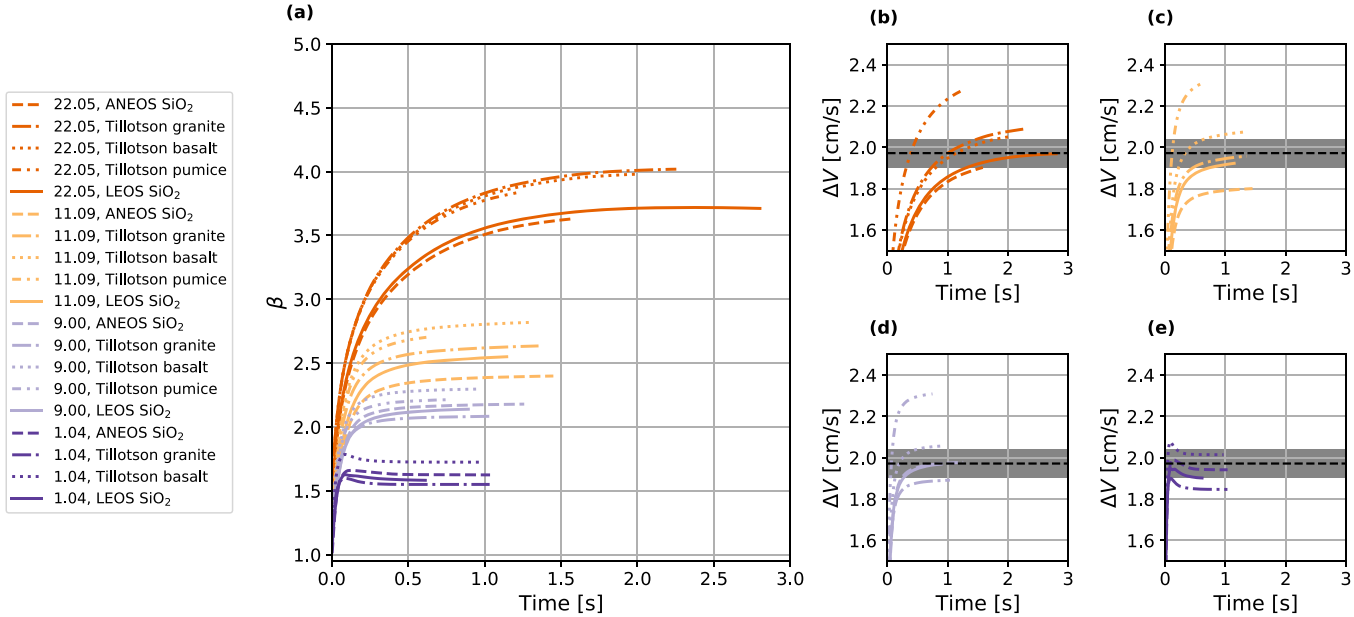

Figure 6. Results of simulations examining the effect of EOS/material choice showing (a) β vs. time, and (b)–(e) ΔV vs. time. Lines are colored to group simulations with the same material input parameters, and line type indicates the EOS and material choice. The dashed black lines in plots (b)–(e) indicate the ΔV of the truth simulation, with the dark gray line covering ± 0.07 cm s^{-1}. Numbers in the legend (e.g., 22.05) are simulation IDs (see Table F1).

The crater of the CTH truth simulation was measured at 0.1 s (the final time step of that simulation) and had a width of 9.2 m and a depth of 6.9 m. While the crater depth of the truth simulation falls directly on the general trend observed in our simulations, the crater width of the truth simulation is significantly smaller. This difference is observable both in the general trend of crater width versus Y_{s0} as well as crater size ratio versus ϕ (Figure 7). The underestimation of crater size relative to the Spheral simulations likely results from the transient nature of the crater in the CTH simulation. When measuring crater size in the Spheral simulations, we specifically attempted to predict a late-time crater shape by removing material below a critical density after ΔV stabilized. For the majority of crater shapes in our simulations, the change in width between the transient crater and the predicted final crater is larger than the change in depth. Thus, we expect that the predicted final crater in the truth simulation would similarly demonstrate a large increase in crater width relative to the transient with only a small increase in crater depth, bringing the truth simulation crater size into relative alignment with the trends we observe.

Given the transient nature of the truth simulation crater, it is difficult to use crater size as a precise constraint on our simulations (compared to the easily quantified asteroid mass, for instance). In the interest of exploring how crater size might narrow the range of possible material properties, however, we can make a qualitative comparison. Thus, for successful simulations, we examine the transient crater size at 0.1 s relative to the predicted crater size. The results are plotted as empty symbols in Figure 7.

Unsurprisingly, the transient crater sizes at 0.1 s are all smaller than the craters predicted from the final time steps of our simulations, and thus the truth simulation lines up with the transient crater sizes quite well (Figure 7(a)). While there is a relationship between the transient crater size and Y_{s0}, it is much weaker than the relationship between predicted crater size and Y_{s0}. In fact, for simulations with asteroid masses within 10% of the truth simulation, all of the transient crater widths are within 15% of the truth simulation crater width. Thus, our results suggest that the early transient crater size does not significantly improve constraints on the material properties of the asteroid, but the final crater appears diagnostic in conjunction with ΔV.

5.4. Deflected or Disrupted?

When post-impact asteroid velocities are as large as the ones discussed in this study, the likelihood of disruption rather than deflection is an additional important caveat. An asteroid velocity change of 10% of the escape velocity is commonly considered a safe threshold for deflection (e.g., Dearborn & Miller 2015), but the ΔV of the truth simulation is nearly 40% of the escape velocity estimated for Dimorphos (5 cm s^{-1}). The more porous asteroids considered in this study would have even lower escape velocities, making the truth simulation ΔV as high as 73% of escape velocity for the most porous asteroids. The geometry of the inverse test, with the impact vector perpendicular to the long axis of an asteroid with a large aspect ratio, also increases the probability of the asteroid breaking into distinct pieces.

Within the set of successful simulations, the possibility of disruption is particularly stark for the largest craters, where the diameter of the crater rim approaches the length of the minor axis of the model asteroid. In these cases, a large proportion of the asteroid (up to more than 50%) is damaged, with only minor regions of undamaged material a significant distance from the impact site. When the strength of damaged material is low, the large regions of damaged material are unlikely to remain coherent long after impact because of minor variations in velocity across the asteroid body.

While a detailed discussion of disruption is beyond the scope of this study, it is informative to examine the successful simulations for the probability of disruption. We assume that an asteroid that is >25% damaged at the final analyzed time step would be at risk of disruption as the damaged regions in these simulations transect the entire diameter of the asteroid along the

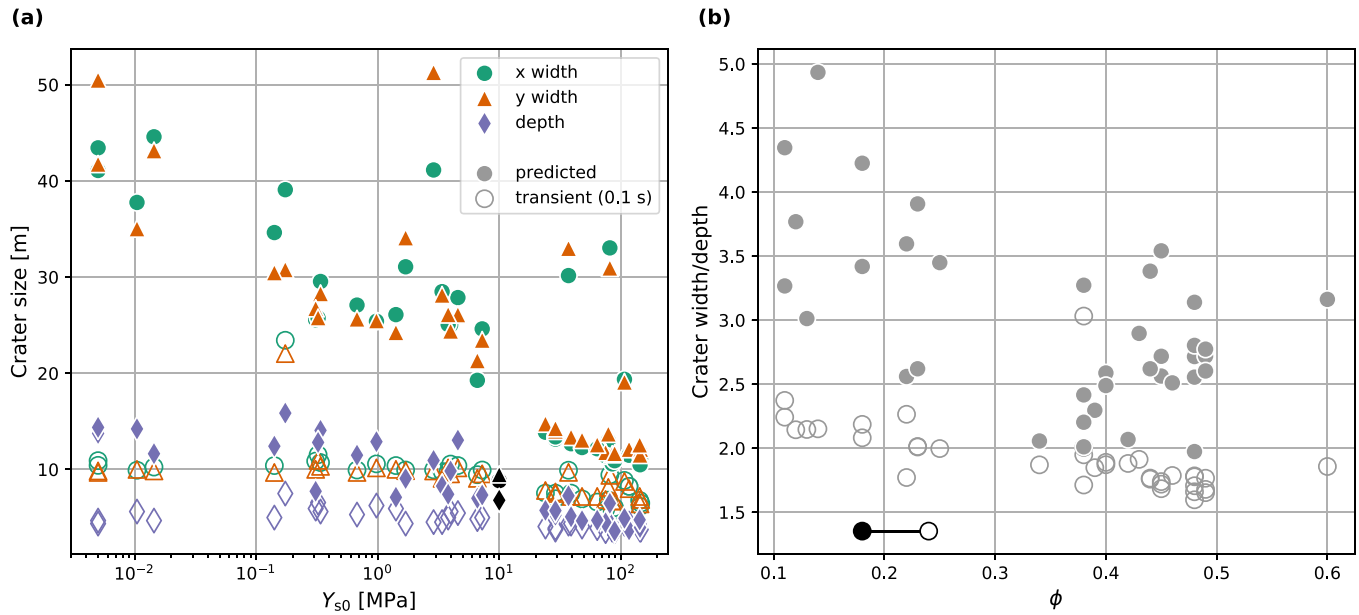

Figure 7. (a) Crater size vs. Y_{s0} for successful simulations. Solid symbols represent the crater estimated from the final simulated time. Empty symbols represent the crater estimated at 0.1 s. The truth simulation is shown in black. (b) The ratio of crater width to crater depth vs. ϕ. Solid and empty symbols have the same interpretation as in (a). The truth simulation is shown in black, with an empty symbol for the 24% porosity set for the basalt EOS of the truth simulation and a solid symbol for the 18% porosity required for an SiO_2 EOS to have the same bulk density.

impact axis. Among the successful simulations, six meet this criterion for disruption risk. This set includes the four solutions with large craters and low values of Y_{s0}. However, similarly large craters that occur at larger values of Y_{s0} have much smaller regions of damaged material. In fact, there is no single parameter that determines the extent of the damaged region. For instance, high porosities are generally associated with smaller damaged regions in our simulations, and no simulation in our disruption-risk set with a ΔV close to the truth simulation has a porosity greater than 0.4. However, there is not a direct correlation between porosity and damage extent. Similarly, while the set of successful simulations at risk of disruption includes the four simulations with the lowest values of Y_{s0}, two simulations with higher values of Y_{s0}, including one with $Y_{s0} = 107$ MPa, are also at high risk of disruption. Additional work is necessary to establish disruption metrics, including the effects of asteroid geometry and material properties on disruption probability.

In terms of the DART mission, however, we should emphasize again that the scenario presented in this test involves a significantly larger deflection than we expect in the actual DART experiment. This discrepancy largely results from the fact that the asteroid shape model used here is much smaller than the best estimates for Dimorphos (Naidu et al. 2020). Based on the best available models for Dimorphos, we do not expect disruption to occur in the DART impact, though recent models of DART-like impacts into extremely low-strength targets indicate the possibility of global resurfacing (Raducan & Jutzi 2022).

6. Implications for DART and Planetary Defense

The results of this inverse test demonstrate the importance of knowing as much as possible about the asteroid target prior to attempting a kinetic deflection, particularly the asteroids mass, porosity, strength, and elastic properties. The results of this study describe a wide breadth of possible asteroid responses when the target volume, target shape, target material, impactor mass, impactor strength, and impactor velocity are defined. The velocity changes for our asteroid simulations, modeled across the inverse test as SiO_2, vary from -0.89 to $-4.6\,\mathrm{cm\,s^{-1}}$ depending on the properties ascribed to the asteroid. Even when the mass of the target asteroid is constrained to $\pm 10\%$ of the truth simulation asteroid mass, the range of velocity changes is still $-0.89\,\mathrm{cm\,s^{-1}}$ to $-3.3\,\mathrm{cm\,s^{-1}}$. Similarly, for successful simulations, with asteroid velocities close to the target ΔV, there are a wide range of properties, with strengths ranging from a few kilopascals to more than more than 100 MPa and porosity ranging from 0.11–0.60.

Our inverse test results also demonstrate the need for robust extrapolations for ΔV and β, or, at the very least, robust metrics for choosing final values of ΔV and β. In the DART impact, ΔV will be measured in the weeks following impact, and for theoretical planetary defense missions, the efficacy of a kinetic deflection may be determined over months to years. However, running hydrocodes out to even a few seconds after impact can take days to weeks depending on the material parameters, problem scale, simulation resolution, and available resources. The late-time behavior of a body post-impact (e.g., a velocity change due to slow-moving ejecta) may be critical when planning deflection missions.

Additional information will be available from the DART mission that was not used in the inverse test. In addition to the mass estimate and crater observations by Hera discussed above, LICIACube will follow a few minutes behind the DART spacecraft to image the ejecta cone (Dotto et al. 2021). We did not utilize information about the ejecta cone in the inverse test in order to model what can be learned from the minimum DART mission requirements, but the size and morphology of the ejecta cone may help constrain many properties. In particular, the ejecta cone images may easily rule out extreme material properties, when either a minuscule or massive amount of ejecta is produced. In addition, the ejecta behavior may provide information about the shallow subsurface makeup of

Dimorphos. For instance, a large boulder directly below the impact site would likely decrease the amount of ejecta produced.

The general results of this study, e.g., the trends identified between the deflection magnitude and asteroid material parameters as well as the degeneracy associated with predicting material properties from a single observation, will be applicable to the DART impact regardless of the nature of the target body, Dimorphos. However, the precise numbers used and generated in this study are not expected in the DART impact. For instance, previous work shows that using a sphere as an impactor leads to a larger ΔV than would be expected from the DART spacecraft, with a sphere overestimating ΔV by up to 25% (Owen et al. 2022; Raducan et al. 2022). Another oversimplification in the models presented here is modeling the internal structure of the asteroid as homogeneous: rubble-pile structures can have important effects on ejecta production (e.g., Stickle et al. 2017; Graninger et al. 2021). Finally, the Itokawa shape model in this study was small relative to the prediction for Dimorphos, leading to larger deflections than predicted for DART. Thus, the expected risk for disruption or destabilization of the orbit of Dimorphos around Didymos is low.

While the miniature Itokawa simulated for the inverse test is likely small compared to Dimorphos, it is large enough to potentially require mitigation efforts were it on an impact trajectory with Earth. Depending on the albedo of this theoretical Dimorphos-sized hazardous object, the warning time in such a scenario could be short, requiring a deflection of the magnitude used for this inverse test and thus a nonnegligible risk of disruption. The results of this study suggest that, in addition to understanding the effects of asteroid material properties, the role of asteroid geometry and impact location may be critical in analyzing disruption risk.

At the moment, significant uncertainties remain in the possible assemblages of material properties for hazardous asteroids, and, apart from computational studies, we know little about how these properties will affect kinetic deflection outcomes. DART will provide an essential first glimpse at this technology's potential, but its applicability across the diverse population of near-Earth asteroids will remain uncertain without future reconnaissance and mitigation demonstration missions. As emphasized in the 2023–2032 Planetary Science and Astrobiology Decadal Survey (National Academies of Sciences, Engineering, and Medicine 2022), the ability to demonstrate rapid reconnaissance of asteroids will provide an important link between discovery and design of optimal mitigation missions. The computational study presented here provides further support for the importance of pre-mitigation characterization data on specific asteroid targets, while reinforcing the need to characterize the geotechnical properties of more near-Earth asteroids in general. The more information we have on likely impact scenarios prior to a potential deflection, the more likely a mission to defend the planet will be successful.

This work was supported by the DART mission, NASA Contract No. 80MSFC20D0004. Lawrence Livermore National Laboratory is operated by Lawrence Livermore National Security, LLC, for the U.S. Department of Energy, National Nuclear Security Administration under Contract DE-AC52-07NA27344. LLNL-JRNL-837536. This work was also supported in part by the Advanced Simulation and Computing (ASC)–Verification and Validation program and ASC–Integrated Codes program at Los Alamos National Laboratory and a Chick Keller Postdoctoral Fellowship in Earth and Space Science from the Center for Space and Earth Science at Los Alamos National Laboratory. Los Alamos National Laboratory, an affirmative action/equal opportunity employer, is operated by Triad National Security, LLC, for the National Nuclear Security Administration of the U.S. Department of Energy under contract 89233218NCA000001. LA-UR-22-28492.

Appendix A
The Truth Simulation

The shape model used in this study to represent Dimorphos was a miniature Itokawa, with a total volume of 276,386 m^3 and a resolution of 2.31 m per facet. The model was provided in a reference frame such that the positive X-direction was pointed away from the Didymos primary asteroid and the positive Y-direction was parallel to the orbital velocity of Dimorphos (Figure A1). In this reference frame, the impact location was at $(5.57 \times 10^{-5}, 0.029025, -0.01614)$ km, placing the impact location on a crater wall. The spacecraft velocity at impact was $(-0.012, -6.314, 3.511)$ km s^{-1}. For the Spheral simulations, we rotated the simulation setup such that the spacecraft velocity was oriented in the negative Z-direction for convenience; the Spheral reference frame is shown in Figure 1.

A.1. CTH

CTH is a two-step Eulerian shock physics hydrocode developed and maintained by Sandia National Laboratories (McGlaun et al. 1990). The CTH truth simulation uses a SESAME (Lyon & Johnson 1992) aluminum EOS to describe the impactor and an SESAME basalt EOS to describe the asteroid. The impactor has a radius of 36.51 cm, a mass of 612 kg, a von Mises strength of 275 MPa, and a tensile fracture strength of 310 MPa. The behavior of the asteroid is represented using a von Mises strength model with a strength of 10 MPa, a tensile fracture strength of 10 MPa, and a Johnson-Cook damage model with failure at a strain of 0.05. Porosity is modeled using a pressure-alpha model using parameters from Jutzi et al. (2008). The resolution of the simulation is set to 3 cells per projectile radius (cppr) on a flat mesh.

A.2. FLAG

Free LAGrange (FLAG) is a multiphysics arbitrary Lagrangian-Eulerian code maintained by Los Alamos National Laboratory (Burton 1992, 1994a, 1994b). FLAG has been verified and validated for impact crater and high-velocity impacts and has been used to study planetary science applications (Caldwell et al. 2018, 2020, 2021; Caldwell 2019). The FLAG truth simulation uses a Mie-Grüneisen EOS for both the aluminum impactor as well as the basalt asteroid. Porosity is described with a pressure-alpha model, artificial viscosity with a von Neumann Richtmeyer formulation with $q2 = 1.3$ and $q1 = 0.3$, and damage with a Johnson-Cook model with $d1 = 0.05$ (Johnson & Cook 1985). A Tipton closure model is used to handle mixed-material zones. The resolution of the simulation ranged from 7.3 cm (5 cppr) at the impact site to 1 m (0.37 cppr) away from the impact.

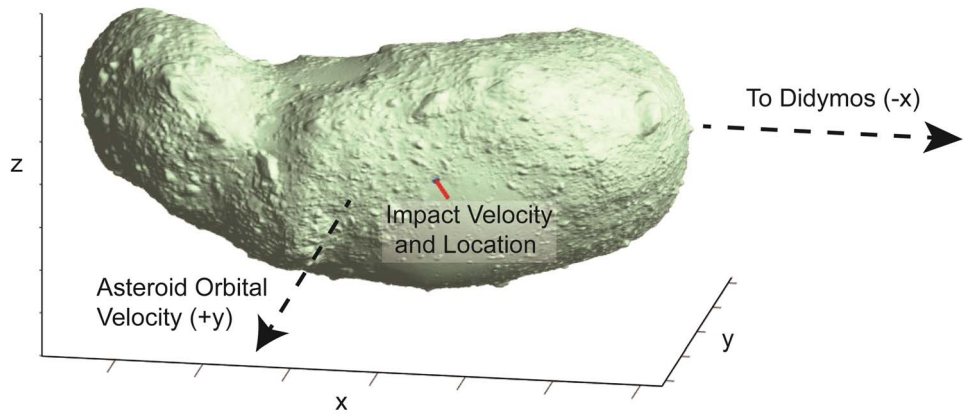

Figure A1. Initial reference frame for this study, showing the shrunken Itokawa shape model and indicating the impact velocity vector (in red), the impact location (in blue), the vector toward the Didymos primary asteroid, and the vector of the asteroid's orbital velocity.

Appendix B
Spheral Material Models and Metrics: Additional Information

B.1. Material Models

We use a fifth-order B-spline kernel, and our adaptive smoothing length algorithm maintains roughly four radial neighbors spanning the extent of the kernel (Owen 2010). This equates to roughly 268 neighbors in three dimensions. We use Monaghan–Gingold (Monaghan & Gingold 1983) artificial viscosity with linear coefficient, $Cl = 1.5$, and quadratic coefficient, $Cq = 0.75$. Strength and shear modulus are modified by the porosity as $n = n_0(1 - \phi)$, with n being either the strength or shear modulus of intact or damaged material. The coefficient of internal friction is set to 1.2 for intact material and 0.6 for damaged material.

In our strain–porosity model, compaction is treated as elastic up to a strain of -1.88×10^{-4}, beyond which the compaction is modeled as exponential with an exponential compaction factor $\kappa = 0.9$. In our damage model, our flaw distribution is governed by the proportional and exponential Weibull constants, k and m, respectively. Flaws become active and propagate damaging the material once their activation strain is exceeded. In this paper, we set k and m equal to 5.00×10^{24} and 9.0, respectively. The activation strain is calculated using Spheral's "Pseudo Plastic Strain" option. This involves using the time-derivative of deviatoric stress and the shear modulus to integrate the activation strain in time. Additional details regarding the damage model and the parameters used can be found in Owen et al. (2022).

The impactor is modeled as a solid aluminum sphere with no porosity and a radius of 37.8 cm (calculated from the density of solid aluminum at 2.7 g cm^{-3} and an impactor mass of 612 kg). Most simulations in this paper use a Livermore Equation of State (LEOS) aluminum EOS to describe the impactor and an LEOS SiO_2 EOS to describe the asteroid (Fritsch 2016). Simulations testing EOS choice use either an LEOS aluminum EOS or a Tillotson aluminum EOS to describe the impactor (the choice of impactor EOS had little effect on the impact simulation). Asteroid EOS and material combinations for these simulations are ANEOS SiO_2 (Thompson 1990), Tillotson basalt, Tillotson granite, and Tillotson pumice (Tillotson 1962). Parameters used in the Tillotson EOS for different phases can be found in Table B1.

Table B1
Parameters Used in Tillotson EOS

Parameter	Material		
	Basalt	Granite	Pumice
ρ_0 (g cm^{-3})	2.700	2.680	2.327
a	0.5	0.5	0.5
b	1.5	1.3	1.5
A (dyne cm^{-2})	2.67e11	1.80e11	2.67e11
B (dyne cm^{-2})	2.67e11	1.80e11	2.67e11
α	5.0	5.0	5.0
$\beta_{\rm EOS}$	5.0	5.0	5.0
ε_0 (erg g^{-1})	4.87e12	1.60e11	4.87e12
$\varepsilon_{\rm liquid}$ (erg g^{-1})	4.72e10	3.50e10	4.72e10
$\varepsilon_{\rm vapor}$ (erg g^{-1})	1.82e11	1.80e11	1.82e11

Note. $\beta_{\rm EOS}$ is a parameter in the Tillotson EOS (Tillotson 1962) and is entirely separate from the momentum enhancement factor β discussed in this paper.

B.2. Ejecta Definition

Many hydrocodes define ejecta using two filters: velocity and spatial location. The first filter checks that the velocity of the material is greater than the escape velocity for the target being struck. The second filter is a plane above the asteroid surface with a normal parallel to the spacecraft velocity vector. Material above the plane moving faster than the escape velocity is considered ejecta and contributes to the ejecta momentum (Figure B1(a)).

We used a planar filter for ejecta at the outset of this study. However, the geometry of the shrunken Itokawa asteroid meant that a portion of the early ejecta traveled at a shallow angle relative to the spacecraft velocity vector. This trajectory meant this material was not accounted for using the typical ejecta definition (Figure B1(a)). For our simulations, therefore, we incorporated a filter parallel to the asteroid surface, recalculating the results of previous simulations. Material moving faster than the escape velocity and located at least 1 m above the original asteroid surface was labeled as ejecta. In addition to capturing fast-moving low-angle ejecta, this ejecta definition had the added benefit of converging to a stable ΔV and β more quickly (Figure B1(b)). We expect the magnitude of this benefit to be directly related to the geometry of the asteroid and the angle of impact relative to the asteroid surface orientation.

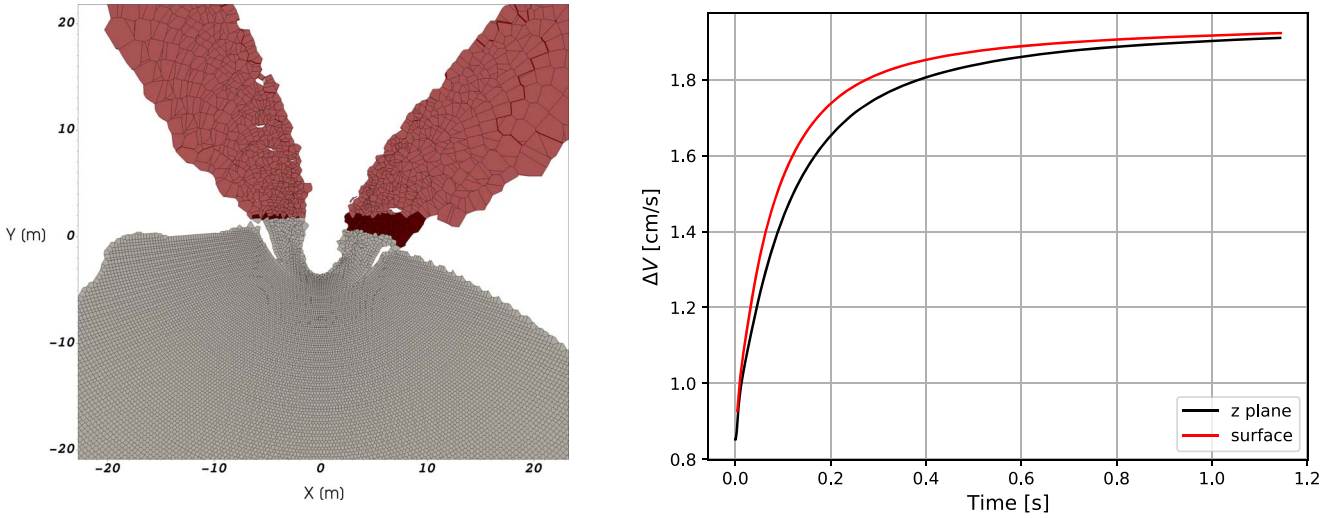

(a) (b)

Figure B1. (a) Example simulation exhibiting the difference in ejecta definition. Material in gray is considered part of the asteroid, and material in light red is considered ejecta in both definitions. The material in dark red is considered ejecta only by our definition using the asteroid surface. (b) ΔV convergence with the old z-plane definition (black) and the new surface definition (red).

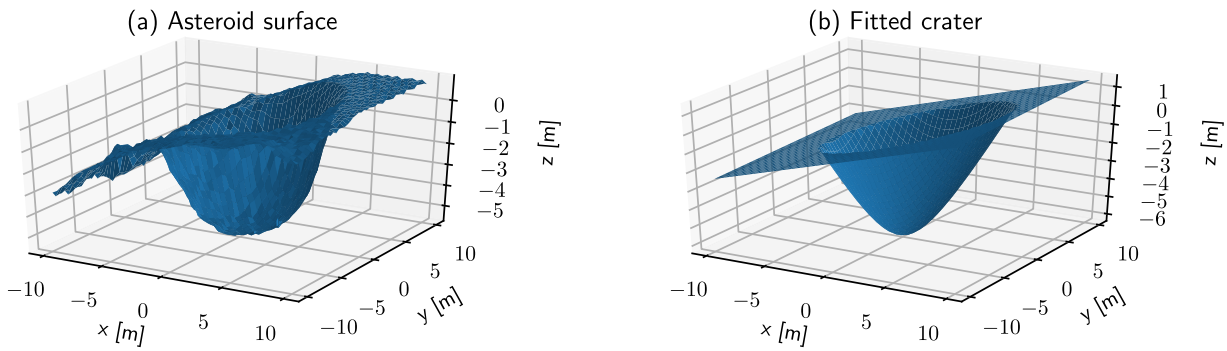

Figure B2. Example of crater fit for simulation 11.09. (a) Original surface of critical density. (b) Plane/hyperboloid fit to the surface.

B.3. Crater Definition

Crater morphology was described for simulations that produced the correct ΔV. Small craters (<20 m in diameter) were fit using a hyperboloid to describe the crater itself and a plane to describe the asteroid surface. The crater depth was defined as the distance between the plane and the hyperboloid below the plane. Crater diameter was defined as the average of the two axes of the ellipse formed by the intersection of the plane and the hyperboloid (Klein 2013). While the craters in the simulations were not always hyperbolic in morphology, the crater depth and diameter fit using this method were accurate for many different crater geometries (Figure B2). For large craters with diameters greater than 20 m, the volume of excavated material was large enough to invalidate the planar assumption for the asteroid surface. In these cases, crater size was measured manually from two perpendicular cross sections.

Appendix C
Using Machine Learning to Examine the Search Space

For the first 138 simulations, Y_{s0} and G_{s0} were set to cover ranges more equivalent to intact or partially fractured rock (Table C1). For the next 120 simulations, however, we focused on weaker materials more similar to sand or clay. The ranges for $P_{\min}$, $P_{d,\min}$, and ϕ did not vary across these first 258 simulations. The final 80 simulations included information on asteroid mass, thus constraining porosity. Other variables in these final simulations were allowed to vary across the full ranges explored in this study.

We set up a machine-learning decision-tree algorithm to direct the parameter choices tested in this study, using the seven material parameters as inputs and ΔV as the output. The algorithm was initially seeded with a set of 40 simulations with randomized parameter combinations (Scan 1). Ten successive scans of 3–16 simulations each were run for the "intact rock" parameters, nine scans of 8–16 simulations each were run for "fractured rock" parameters, and five scans of 16 simulations each were run for the mass-constrained parameters.

For each scan, the algorithm generated between 5000 and 10,000 possible parameter combinations that could potentially produce the correct ΔV using a decision tree with a tree depth of 34. We then selected the simulations for that scan using Mitchell's best sampling algorithm (Mitchell 1991). This selection algorithm uses a k-d tree to find the simulations that are the farthest apart in the seven-dimensional input space. Once the simulations for each scan were run and we were satisfied with the extrapolations for ΔV, the results were added to the training set for the decision-tree algorithm before choosing material parameter combinations for the next scan.

Table C1
Variable Ranges Searched for Simulations

Variable	Strong Intact Rock ($n = 138$)	Weak Fractured Rock ($n = 120$)	Mass Constrained ($n = 80$)
Y_{s0} (MPa)	10^0–$10^{2.2}$ (linear)	10^{-3}–10^0 (logarithmic)	10^{-3}–$10^{2.2}$ (logarithmic)
Y_{d0} (MPa)	10^{-4}–10^0 (linear)	10^{-5}–10^{-1} (logarithmic)	10^{-5}–10^0 (logarithmic)
G_{s0} (GPa)	10^{-1}–10^2 (linear)	10^{-2}–10^1 (logarithmic)	10^{-2}–10^2 (logarithmic)
G_{d0} (GPa)	10^{-3}–10^0 (linear)	10^{-4}–10^0 (logarithmic)	10^{-4}–10^3 (logarithmic)
$-P_{\min}$ (GPa)	10^{-8}–10^{-1} (logarithmic)	10^{-8}–10^{-1} (logarithmic)	10^{-8}–10^{-1}(logarithmic)
$-P_{d,\min}$ (GPa)	10^{-10}–10^{-4} (logarithmic)	10^{-10}–10^{-4} (logarithmic)	10^{-10}–10^{-4} (logarithmic)
ϕ	0.05–0.70 (linear)	0.05–0.70 (linear)	0.10–0.26 (linear)

Note. Whether the search was conducted in linear or logarithmic space is noted for each variable in each simulation set. P_{minute} and $P_{\text{day,minute}}$ are tensile pressures.

We note that we changed the ejecta definition used to calculate ΔV after Scan 17. Details regarding the two ejecta definitions are described in Section B.2. All reported values for ΔV and β are calculated using the new ejecta definition, but the decision-tree algorithm we utilized likely would not reproduce the same material parameter sets tested in this study.

Appendix D
Extrapolations to Large Times

The large parameter space examined in this study necessitates running many simulations to adequately sample the multidimensional space. Thus, due to computational constraints, simulations could not always be run until the system equilibrated. For the purposes of the machine-learning algorithm, we fit curves of ΔV versus time with an exponential decay model. A Gaussian was added to phenomenologically describe the local maximum observed at early times. The curve was fit as:

$$\Delta V = C_1 \times [1 - \exp(-C_2(t + C_3))] + C_4 \times \exp\left[-\frac{(t - C_5)^2}{2C_6}\right], \tag{D1}$$

where t is time, and C_1 through C_6 are fitting constants. ΔV at t_∞ is equal to C_1. Figure D1 depicts the fits to all of the simulations run for the inverse test, demonstrating how we extracted extrapolated values for ΔV and β from simulations that do not run very long. For simulations that significantly undershot or overshot the target ΔV (the blue bar), in particular, these extrapolations gave us more realistic velocity magnitudes to input into the machine-learning algorithm.

The extrapolations we have used here are limited in scope and likely predict convergence at earlier times than expected for true system equilibrium. Even simulations run out to times of >3 s do not capture the slow-moving ejecta that may leave the system at late times. The escape velocity of Dimorphos is estimated to be 5 cm s^{-1}. Since our ejecta definition required material to be at least 1 m above the asteroid surface before it would be calculated as ejecta, the slowest-moving proto-ejecta particles would take at least 20 s to pass this boundary. This would take weeks of computation time on hundreds of processors and would not be usable for the quick turnarounds desired for planetary defense missions, including DART.

That said, while the velocity of this ejecta will clearly be much slower than the ejecta analyzed, significant mass may still escape the asteroid and contribute to a momentum change. For instance, in one simulation of a weak asteroid (22-05), the projected final crater was ~40 m wide and excavated ~15 m down, with ~6% of the asteroid's mass predicted to eventually escape. This is dramatically different from the ~0.46% of mass that had escaped to this point, despite the comparatively flat relationship between ΔV and time. Thus, the overall magnitude of the contribution of this late-stage ejecta must be analyzed in future studies.

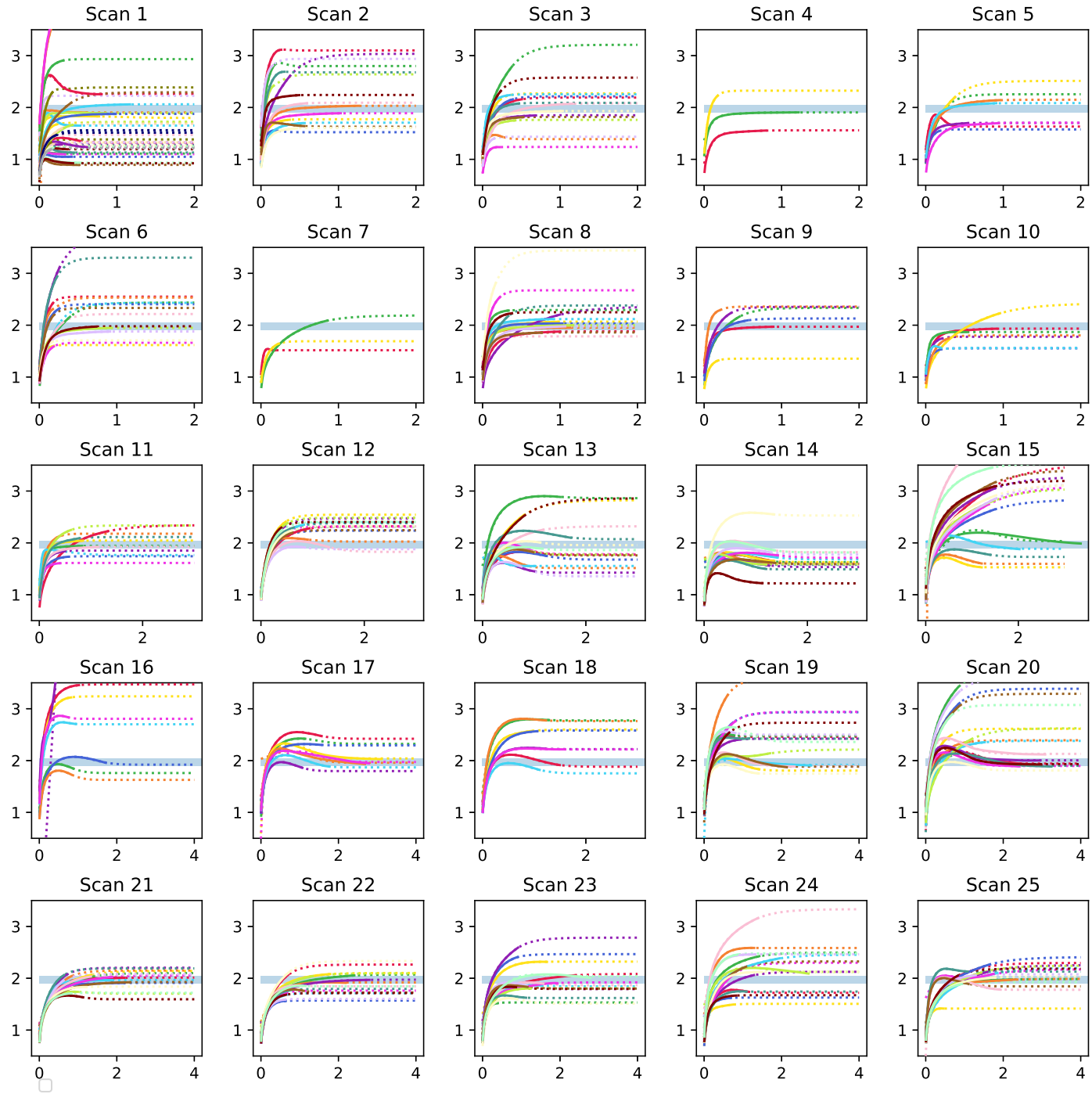

Figure D1. Extrapolations for ΔV for all simulations, with time in seconds on the X-axis and the magnitude of ΔV in centimeters per second on the Y-axis. Solid lines show the data from each simulation, and dotted lines in the same color show the fit of the extrapolation function to those data. The blue bar at the center of each plot shows the target ΔV of 1.972 ± 0.07 cm s^{-1}

Appendix E
Extremes in Behavior

While the exponential decay model used to describe the late-time behavior of our simulations works well for most of our parameter combinations, this is not true for all simulations. Simulations of weak asteroid targets with significant ejecta coming from locations other than the impact site were especially poorly fit by the exponential decay model. The extra ejecta typically decreases ΔV and β in the orbital direction with time, resulting in a lack of convergence with time. For these simulations, reported values for ΔV and β are for the final time step (commonly >2 s), but they are expected to be lower.

One simulation is an extreme outlier, with nearly fluid-like behavior (Figure E1). Many of the parameters for this simulation are well within the ranges describing successful simulations, except for the damaged shear modulus ($G_{d0} = 174$ kPa). This modulus is even smaller than low-density aerogel (e.g., Scherer et al. 1995) and as such is unsuitable for describing a realistic asteroid response.

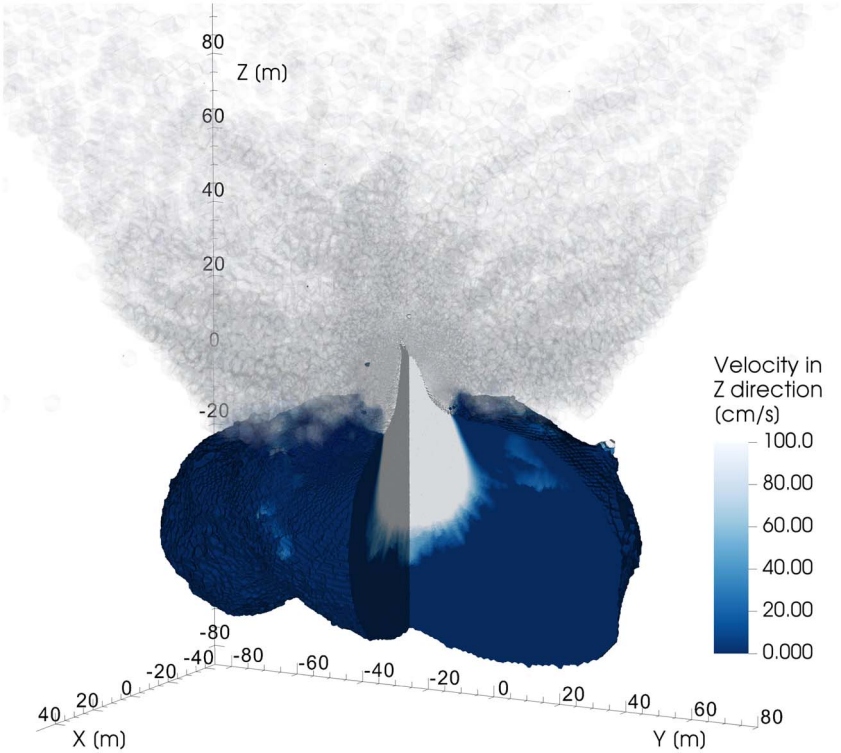

Figure E1. Fluid-like behavior in simulation 16.05. Asteroid material is colored according to its velocity in the *Z*-direction (with white material moving upward at or faster than 1 m s^{-1}). Material with a density below 0.5 g cm^{-3} is shown in translucent black. One-quarter of the simulation visualization is clipped out to show the velocity fields interior to the asteroid.

Appendix F
Additional Supplemental Figures and Results

This appendix contains additional supporting figures (Figures F1 and F2) and tables (Tables F1–F3). Figure F1 shows the results for all simulations similar to Figure 2, with simulations in red having more realistic Poisson's ratios for asteroid material. Figure F2 displays the results of all simulations similar to Figure 4, but with a vertical axis for each material input explored in this study (i.e., including those not set in the truth simulations). Tables F1–F3 contain the inputs and results of all of the simulations and the crater sizes for the simulations with a final ΔV in the target range.

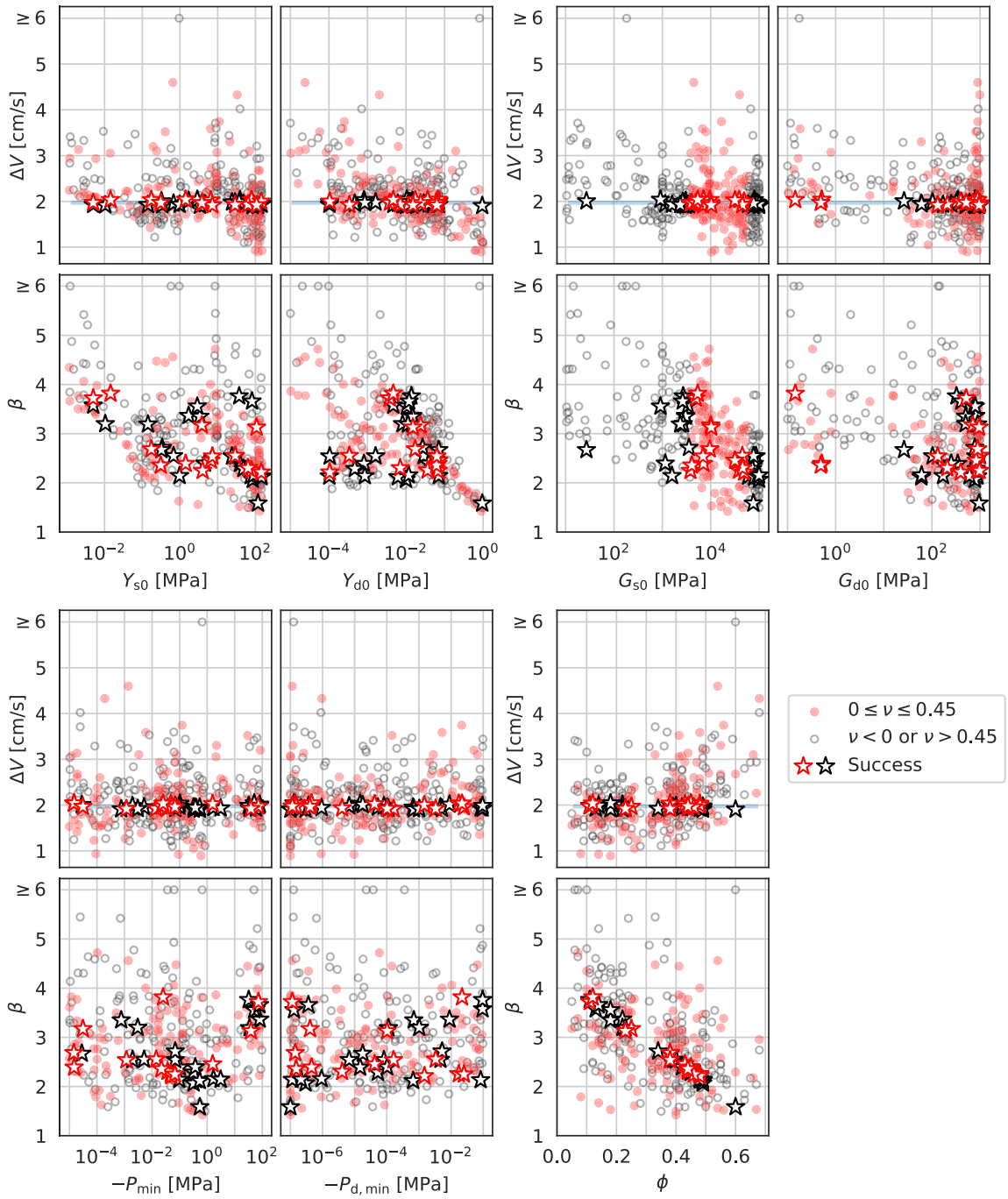

Figure F1. Trends across all simulation results. This figure contains the same simulation results as Figure 2, but points are colored in red for Poisson's ratios between 0 and 0.45 and black for lower or higher Poisson's ratios. Stars indicate simulations with extrapolated values of ΔV in the success range.

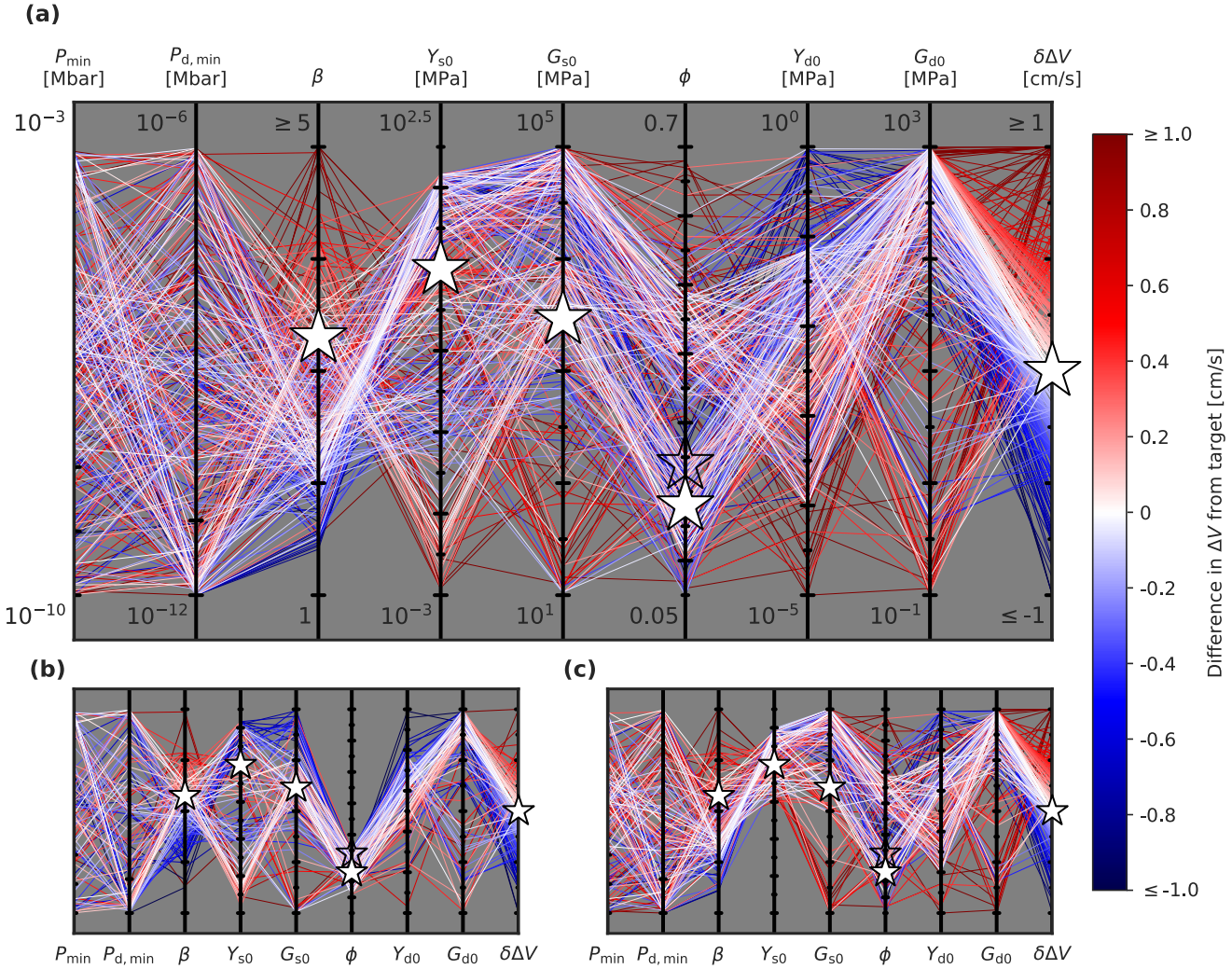

Figure F2. Parallel coordinate plots showing all input variables of the inverse simulations, as well as final ΔV and β. Simulation lines are colored by the difference between the simulation ΔV and the target ΔV, with blue being slower than the truth simulation and red being faster than the truth simulation. White stars indicate the values of the truth simulation. For ϕ, the open star indicates the original truth simulation value of 0.24 while the solid white star indicates the porosity required for an equivalently massive asteroid in our simulations. Plots are shown for (a) all simulations, (b) simulations with initial asteroid mass within 10% of the truth simulation, and (c) simulations with Y_{s0} within 1 order of magnitude of the truth simulation. Ticks and axis limits in (b) and (c) are the same as in (a).

Table F1
Inverse Simulation Inputs and Results

Sim ID	Processors	Run Time (hr)	Sim Time (s)	Y_{s0} (MPa)	Y_{d0} (MPa)	G_{s0} (MPa)	G_{d0} (MPa)	ϕ	P_{min} (MPa)	$P_{d,min}$ (MPa)	Sim ID	$\beta_{t=0.1}$	$\beta_{t=max}$	$\beta_{t=\infty}$	$\Delta V_{t=0.1}$ (cm s^{-1})	$\Delta V_{t=0.2}$ (cm s^{-1})	$\Delta V_{t=max}$ (cm s^{-1})	$\Delta V_{t=\infty}$ (cm s^{-1})
1.00	144	54.2	0.8038	81	0.785	4530	169	0.67	−5.87e−4	0	1.00	1.7958	1.5308	1.5355	−2.5920	−2.5576	−2.2568	−2.2603
1.01	144	38.5	0.2768	64	0.985	100000	380	0.35	−8.38e−4	0	1.01	1.5411	1.4957	1.4951	−1.1353	−1.1170	−1.1113	−1.1112
1.02	144	86.1	0.7703	113	0.375	52200	331	0.52	−2.49e−4	0	1.02	1.8247	1.8548	1.8571	−1.7902	−1.8212	−1.8288	−1.7982
1.03	144	38.3	0.4156	119	0.99	28400	83	0.26	−3.20e−4	0	1.03	1.6932	1.6082	1.6092	−1.0871	−1.0557	−1.0490	−1.0489
1.04	144	76.2	0.6123	117	0.952	76000	953	0.6	−5.42e−4	0	1.04	1.6247	1.5831	1.5835	−1.9458	−1.9361	−1.9021	−1.9035
1.05	144	38.1	0.2900	118	0.716	88000	297	0.41	−6.62e−4	0	1.05	1.5656	1.5805	1.5818	−1.2697	−1.2788	−1.2858	−1.2869
1.06	144	38.6	0.5289	38	0.859	16400	875	0.56	−2.49e−4	0	1.06	1.7659	1.5177	1.5199	−1.8900	−1.7730	−1.6496	−1.6507
1.07	144	38.8	0.3272	50	0.976	64000	36	0.28	−5.48e−5	0	1.07	1.7115	1.6557	1.6572	−1.1276	−1.1065	−1.0993	−1.1000
1.08	144	85.0	0.8513	132	0.286	40200	336	0.52	−2.59e−4	0	1.08	1.8740	1.9276	1.9279	−1.8328	−1.8841	−1.8897	−1.8900
1.09	144	19.3	0.1623	108	0.58	70100	101	0.37	−5.18e−4	0	1.09	1.6870	1.6756	1.6639	−1.2733		−1.2663	−1.2572
1.10	144	38.7	0.4465	131	0.897	22400	622	0.4	−6.71e−4	0	1.10	1.5759	1.4229	1.4213	−1.2519	−1.1772	−1.1301	−1.1312
1.11	144	19.0	0.1516	143	0.602	94000	887	0.63	−2.43e−5	0	1.11	1.6997	1.7196	1.7269	−2.1948		−2.2199	−2.2256
1.12	144	38.8	0.5089	118	0.896	10400	541	0.18	−5.96e−4	0	1.12	1.6795	1.5270	1.5303	−0.9689	−0.9117	−0.8908	−0.8935
1.13	144	19.3	0.1743	103	0.686	58100	352	0.43	−5.73e−4	0	1.13	1.6232	1.5940	1.5833	−1.3563		−1.3342	−1.3242
1.14	144	38.4	0.3587	69	0.871	46100	935	0.4	−3.25e−4	0	1.14	1.5851	1.4934	1.4949	−1.2613	−1.2154	−1.1939	−1.1951

Note. This table is published in its entirety in machine-readable format. A portion is shown here for guidance regarding its form and content. The simulation ID column is repeated here for clarity. The number of computer processors used as well as the computer run time required to reach the final simulation time are reported for each simulation. β is reported at $t = 0.1$ s, $t = t_{max}$, and the extrapolated $t = t_{\infty}$. ΔV is reported at $t = 0.1$ s, $t = 0.2$ s, $t = t_{max}$, and the extrapolated $t = t_{\infty}$.

(This table is available in its entirety in machine-readable form.)

Table F2
Results of Simulations Comparing EOS/Material Choice

Original Sim ID:		1.04		9.00		11.09		22.05	
EOS	Material	ΔV (cm s^{-1})	β	ΔV (cm s^{-1})	β	ΔV (cm s^{-1})	β	ΔV (cm s^{-1})	β
LEOS	SiO_2	−1.90	1.58	−1.97	2.14	−1.92	2.55	−1.97	3.72
ANEOS	SiO_2	−1.94	1.63	−1.98	2.18	−1.80	2.40	−1.93	3.65
Tillotson	basalt	−2.01	1.73	−2.06	2.30	−2.07	2.82	−2.07	4.00
Tillotson	granite	−1.84	1.55	−1.89	2.08	−1.96	2.64	−2.10	4.03
Tillotson	pumice	⋯	⋯	−2.31	2.21	−2.32	2.71	−2.32	3.90

Note. Tillotson pumice not run for simulation 1.04. All values of ΔV and β in this table are extrapolated to $t \sim \infty$, following the method used in the rest of this study.

Table F3
Transient and Final Predicted Crater Dimensions for Successful Simulations

Sim ID	Transient Crater (0.1 s)			Final Predicted Crater		
	x (cm)	y (cm)	z (cm)	x (cm)	y (cm)	z (cm)
1.04[a]	825	801	438	1148	1211	373
2.04[a]	754	719	438	1268	1338	508
3.13[a]	650	688	375	1124	1212	430
4.01[a]	568	672	375	1058	1158	408
6.08[a]	694	719	406	1228	1307	466
6.14[a]	696	766	391	1315	1401	525
8.03[a]	681	813	438	1298	1371	476
8.04[a]	617	642	375	1049	1151	397
8.08[a]	678	719	438	1178	1257	477
8.11[a]	754	781	406	1387	1476	575
9.00[a]	581	688	359	1142	1179	446
10.00[a]	661	719	391	1216	1258	472
11.01[a]	604	674	359	1091	1168	360
11.09[a]	754	751	375	1339	1428	573
12.04[a]	946	907	484	1927	2133	701
13.13	994	969	531	2709	2566	1148
15.01	2343	2205	750	3909	3079	1586
16.03	1072	1032	563	2954	2830	1406
17.02	1041	1001	594	2610	2425	711
17.04	1056	954	563	2502	2440	984
17.07	1087	1001	594	2556	2676	773
19.06	994	954	500	2462	2345	734
20.00	1041	1017	547	2787	2611	1305
20.05	1154	1095	656	2574	2579	1281
20.14	1058	1017	625	2541	2548	1289
21.00	994	987	438	3107	3410	906
21.03	979	907	453	2849	2814	828
21.06	981	1016	500	2508	2612	742
21.12	1043	969	469	4108	4175	1375
22.04	992	1000	563	3776	3504	1422
22.05	1092	985	438	4344	5049	1438
23.07	886	876	438	1937	1909	492
23.15	997	984	453	4114	5128	1094
25.01	992	970	438	3016	3300	727
25.04	944	939	438	3304	3096	648
25.13	1025	985	469	4459	4315	1164
25.15	1041	969	500	3463	3047	1242

Note.
[a] Final predicted crater measured algorithmically.

ORCID iDs

Kathryn M. Kumamoto https://orcid.org/0000-0002-0400-6333
J. Michael Owen https://orcid.org/0000-0003-4796-124X
Megan Bruck Syal https://orcid.org/0000-0003-2776-9955
Jason Pearl https://orcid.org/0000-0002-5340-7272
Cody Raskin https://orcid.org/0000-0003-2914-2240
Wendy K. Caldwell https://orcid.org/0000-0001-6076-5636
Angela M. Stickle https://orcid.org/0000-0002-7602-9120
R. Terik Daly https://orcid.org/0000-0002-1320-2985
Olivier Barnouin https://orcid.org/0000-0002-3578-7750

References

Alderson, A., & Alderson, K. L. 2007, JAerE, 221, 565
Arakawa, M., Saiki, T., Wada, K., et al. 2020, Sci, 368, 67
Asphaug, E., Ostro, S. J., Hudson, R. S., Scheeres, D. J., & Benz, W. 1998, Natur, 393, 437
Benz, W., & Asphaug, E. 1994, Icar, 107, 98
Bruck Syal, M., Michael Owen, J., & Miller, P. L. 2016, Icar, 269, 50
Burton, D. E. 1992, Connectivity structures and differencing techniques for staggered-grid free-Lagrange hydrodynamics, UCRL-JC-110555, Lawrence Livermore National Laboratory, https://www.osti.gov/biblio/10161662
Burton, D. E. 1994a, Consistent finite-volume discretization of hydrodynamic conservation laws for unstructured grids, UCRL-JC-118788, Lawrence Livermore National Laboratory, https://www.osti.gov/biblio/71618
Burton, D. E. 1994b, Multidimensional discretization of conservation laws for unstructured polyhedral grids, UCRL-JC-118306, Lawrence Livermore National Laboratory, https://www.osti.gov/biblio/35336
Caldwell, W. K. 2019, PhD thesis, Arizona State Univ., https://core.ac.uk/display/200249764
Caldwell, W. K., Euser, B., Plesko, C. S., et al. 2021, Applied Sciences, 11, 2504
Caldwell, W. K., Hunter, A., Plesko, C. S., & Wirkus, S. 2018, Journal of Verification, Validation and Uncertainty Quantification, 3, 031004
Caldwell, W. K., Hunter, A., Plesko, C. S., & Wirkus, S. 2020, Icar, 351, 113962
Cheng, A. F., Atchison, J., Kantsiper, B., et al. 2015, AcAau, 115, 262
Cheng, A. F., Michel, P., Jutzi, M., et al. 2016, P&SS, 121, 27
Cheng, A. F., Rivkin, A. S., Michel, P., et al. 2018, P&SS, 157, 104
Collins, G. S., Melosh, H. J., & Ivanov, B. A. 2004, M&PS, 39, 217
Collins, G. S., Melosh, H. J., & Wünnemann, K. 2011, IJIE, 38, 434
Cotto-Figueroa, D., Asphaug, E., Garvie, L. A. J., et al. 2016, Icar, 277, 73
Daly, R. T., Ernst, C. M., Barnouin, O., et al. 2022, PSJ, 3, 207
Dearborn, D. S. P., & Miller, P. L. 2015, in Defending Against Asteroids and Comets, ed. J. N. Pelton & F. Allahdadi (Berlin: Springer), 733
Dearborn, D. S. P., Bruck Syal, M., Barbee, B. W., et al. 2020, AcAau, 166, 290
Dotto, E., Della Corte, V., Amoroso, M., et al. 2021, P&SS, 199, 105185
Feldhacker, J. D., Jones, B. A., Doostan, A., Scheeres, D. J., & Bruck Syal, M. 2017, JGCD, 40, 2417
Fletcher, Z. J., Ryan, K. J., Maas, B. J., et al. 2018, Proc. SPIE, 10698, 106981X
Flynn, G. J., Consolmagno, G. J., Brown, P., & Macke, R. J. 2018, ChEG, 78, 269
Fritsch, F. N. 2016, LIP: The Livermore Interpolation Package, Version 1.6 LLNL-TR-406719-REV-5, Lawrence Livermore National Laboratory, https://www.osti.gov/biblio/1234602
Fujiwara, A., Kawaguchi, J., Yeomans, D. K., et al. 2006, Sci, 312, 1330
Grady, D. E., & Kipp, M. E. 1980, International Journal of Rock Mechanics and Mining Sciences & Geomechanics Abstracts, 17, 147

Graninger, D. M., Stickle, A. M., & Bruck Syal, M. 2021, in 7th IAA Planetary Defense Conf. (Paris: IAA), 195
Holsapple, K. A., & Housen, K. R. 2012, Icar, 221, 875
Ji, S., Li, L., Motra, H. B., et al. 2018, JGRB, 123, 1161
Ji, S., Wang, Q., & Li, L. 2019, Tectp, 766, 270
Johnson, G. R., & Cook, W. H. 1985, EnFM, 21, 31
Jutzi, M., Benz, W., & Michel, P. 2008, Icar, 198, 242
Jutzi, M., & Michel, P. 2014, Icar, 229, 247
Kimberley, J., & Ramesh, K. T. 2011, M&PS, 46, 1653
Kimura, M. 2006, J. Acoust. Soc. Am., 120, 699
Klein, P. P. 2013, AMat, 4, 40
Lyon, S. P., & Johnson, J. D. 1992, SESAME: The Los Alamos National Laboratory Equation of State Database LA-UR-92-3407, Los Alamos National Laboratory, https://www.lanl.gov/org/ddste/aldsc/theoretical/physics-chemistry-materials/_assets/docs/LAUR-92-3407.pdf
McGlaun, J. M., Thompson, S. L., & Elrick, M. G. 1990, IJIE, 10, 351
Meyers, M. A. 1994, Dynamic Behavior of Materials (New York: John Wiley and Sons, Inc), 688
Michel, P., Kueppers, M., Sierks, H., et al. 2018, AdSpR, 62, 2261
Mitchell, D. P. 1991, Computer Graphics, 25, 157
Monaghan, J. J., & Gingold, R. A. 1983, JCoPh, 52, 374
Mordensky, S. P., Villeneuve, M. C., Kennedy, B. M., et al. 2018, JVGR, 359, 1
Moyano-Cambero, C. E., Pellicer, E., Trigo-Rodríguez, J. M., et al. 2017, ApJ, 835
Naidu, S. P., Benner, L. A. M., Brozovic, M., et al. 2020, Icar, 348, 113777
National Academies of Sciences, Engineering, and Medicine 2022, Origins, Worlds, and Life: A Decadal Strategy for Planetary Science and Astrobiology 2023–2032 (Washington, DC: The National Academies Press)
Onur, M. I., Tuncan, M., & Tuncan, A. 2014, in Second European Conf. Earthquake Engineering and Seismology (Istanbul August 2014), www.eaee.org/Media/Default/2ECCES/2ecces_eaee/829.pdf
OSTP 2018, National Near-Earth Object Preparedness Strategy and Action Plan, Office of Science and Technology Policy, https://www.nasa.gov/sites/default/files/atoms/files/ostp-neo-strategy-action-plan-jun18.pdf
Owen, J. M. 2010, in 5th Int. SPHERIC SPH Workshop (Manchester, UK, June 2010), https://www.osti.gov/biblio/1009644
Owen, J. M., DeCoster, M. E., Graninger, D. M., & Raducan, S. D. 2022, PSJ, 3, 218
Owen, J. M., Villumsen, J. V., Shapiro, P. R., & Martel, H. 1998, ApJS, 116, 155
Raducan, S. D., Davison, T. M., & Collins, G. S. 2020, P&SS, 180, 104756
Raducan, S. D., Davison, T. M., Luther, R., & Collins, G. S. 2019, Icar, 329, 282
Raducan, S. D., & Jutzi, M. 2022, PSJ, 3, 128
Raducan, S. D., Jutzi, M., Davison, T. M., et al. 2022, IJIE, 162, 104147
Rivkin, A. S., Chabot, N. L., Stickle, A. M., et al. 2021, PSJ, 2, 173
Scherer, G. W., Smith, D. M., Qiu, X., & Anderson, J. M. 1995, JNCS, 186, 316
Stickle, A. M., Rainey, E. S. G., Bruck Syal, M., et al. 2017, Procedia Engineering, 204, 116
Stickle, A. M., Bruck Syal, M., Cheng, A. F., et al. 2020, Icar, 338, 113446
Stickle, A. M., Burger, C., Caldwell, W. K., et al. 2022, PSJ, in press (arXiv:2209.06659)
Thompson, S. L. 1990, ANEOS analytic equations of state for shock physics codes input manual, SAND-89-2951, Sandia National Laboratory, https://www.osti.gov/biblio/6939284
Tillotson, J. H. 1962, Metallic Equations of State for Hypervelocity Impact, GA-3216, Air Force Weapons Lab
Walsh, K. J. 2018, ARA&A, 56, 593
Wollner, U., Vanorio, T., & Kiss, A. M. 2018, IJSS, 130–131, 211
Wünnemann, K., Collins, G. S., & Melosh, H. J. 2006, Icar, 180, 514